



TECHNISCHE  
UNIVERSITÄT  
WIEN  
Vienna | Austria

# Dissertation

On the electrochemistry of YSZ/Ni and  
related model electrodes

ausgeführt am

Institut Chemische Technologien und Analytik,  
FB Elektrochemie,  
der Technischen Universität Wien

unter Anleitung von

Univ.-Prof. Dipl.-Phys. Dr. Jürgen Fleig und  
Univ.Ass. Dipl.-Ing. Dr.techn. Alexander Karl Opitz

durch

DI Michael Doppler

Matrikelnummer: 00928659

Brigittaplatz 14

A-1200 Wien

Wien, am 08.05.2018

*We are what we repeatedly do. Excellence, then, is not an act, but a habit.*

—William James Durant, *The Story of Philosophy*



# Preface

These lines, while the first a curious reader may see, are the last the author puts his keyboard to work for. From the vantage point of having already written the technical part of this thesis, I highly commend any inquiring spirit venturing to read and understand this thesis in full. But regardless of whether the reader may wish to read the whole monograph or just searches for some data or insight, the mere fact that this work has significance for a reader infuses me with gratitude.

Besides the reader, I of course also want to thank everyone who helped me get to this point. First up, I want to thank Univ.Prof. Jürgen Fleig, Dr. Alexander Opitz and PD Dr. Martin Bram for the guidance and scientific input and for establishing and running the physical laboratory and the research project that enabled this thesis in the first place. In the same breath I wish to thank the representatives from the corporate partners of the CD laboratory, Dr. Marco Brander, Dr. Wolfgang Schafbauer, DI Jürgen Rechberger, and DI Jörg Mathé for coordinating the project and attentively listening to my presentations and providing input, even if the content was often not directly relevant to their work.

For the great collaborations and discussions I want to also thank the other colleagues of the project: Matthias Gerstl, Andreas Nennung, Daniel Röhrens, Florian Thaler, David Udomsilp, Alexander Beez, Katharina Fitzek, Clemens

Antzböck, and Christopher Herzig. The project would have certainly not been the same without them.

Special thanks also to the colleagues in the electrochemistry division for contributing their part to an amazing working climate, especially Alex ‘the Beekeeper’ Opitz, Matthias ‘trivia Wikipedia’ Gerstl, Ghislan ‘Tschisi’ Rupp (IP-gate shall not be forgotten!), Andreas ‘Plüsch’ Welzl & Christoph ‘Plausch’ Slouka, Maximilian ‘the Network’ Morgenbesser, Kurt ‘sonst Kurt’ Horvath and Udo ‘Starling’ Starzacher, and also to Andi, Sandra, Sabine, Stefan, Gregor, Georg, the other Alex, the other other Alex, the other other other Alex, Markus, Steffi, Tobi, Christopher, Edi, Harald, Richard, Jie, Tzveti, Andi, and everyone else I did not mention here.

Finally, I want to thank my family for enabling me to get all the way to writing this line, and especially my fiancée Thao. Writing a dissertation is a marathon, and you helped me run it all the way to the end in best shape.

## Abstract

Solid oxide fuel cells (SOFCs) are highly efficient and clean electrochemical energy converters capable of utilizing a wide variety of fuel infrastructures. Since SOFC performance is influenced by anode performance, structural and electrochemical degradation of the anode during operation is critical in determining the efficiency and lifetime of some types of SOFC systems. In this thesis model anode electrodes, consisting of structured metal thin film electrodes on yttria stabilized zirconia (YSZ), are employed to investigate the reaction mechanism for hydrogen oxidation in SOFC anodes. Using electrochemical impedance spectroscopy two properties were extracted from the system: The electrode interface capacitance and the polarization resistance. The main emphasis is put on YSZ/Ni as the standard anode material for SOFCs.

For the capacitive properties of the YSZ/Ni system significant deviation from the classical Stern double layer model were found for the area specific capacitance value, the bias voltage behavior and the sensitivity towards hydrogen, water, and hydrogen sulfide partial pressures. These deviations can be reconciled by assuming a battery type ‘chemical’ capacitance, in which a voltage driven redox reaction creates a charge buffer. A variety of possible mechanisms for such a chemical capacitance in the YSZ/Ni system are discussed.

Electrocatalytic properties were investigated with the polarization resistance measured by impedance spectroscopy. The source of this electrocatalysis was investigated using electrodes with varying triple phase boundary (TPB) length (but constant area) and electrodes with varying area (but constant TPB length). Measurements on the electrode series with varying TPB length showed that a part of the activity originated from the TPB. Using the electrode series with varying area the unaccounted activity could clearly be attributed to a previously unknown area-related reaction pathway for hydrogen oxidation on YSZ/Ni electrodes. Variation of temperature, hydrogen and water partial pressures, and addition of hydrogen sulfide further solidified the proposed area pathway and showed the different chemical properties of the reaction pathways. Using experimental data two possible reaction mechanisms for the newly found area pathway were proposed.

To further broaden the knowledge base for hydrogen reaction mechanisms on metal/ceramic electrocatalysts, experiments described above for YSZ/Ni were carried out for the following material combinations: YSZ/Pt, scandia doped zirconia/Ni, and titania/Ni. The results showed

that both the metal and ceramic phase influence the electrochemical properties, showing that the metal phase does not merely act as a current collector. The results, combined with literature data, further indicate that catalytic activity of model electrodes is either controlled by the state of the electrolyte surface or by foreign phases in the TPB region.

## Zusammenfassung

Festoxidbrennstoffzellen (SOFCs) sind hocheffiziente und schadstoffemissionsarme elektrochemische Energiewandler, die zudem mit einem breiten Spektrum an Brennstoffen betrieben werden können. Da die Leistung von SOFCs zum Teil durch die Anodeneigenschaften bestimmt wird, ist strukturelle und elektrochemische Degradation der Anode ein kritischer Faktor, der die Effizienz und Lebensdauer mancher SOFC-Bauarten bestimmt. In dieser Arbeit werden Modellelektroden, die aus strukturierten metallischen Dünnschichten auf Yttrium stabilisiertem Zirkonoxid (YSZ)-Substraten bestehen, verwendet um den Reaktionsmechanismus der Wasserstoffoxidation in SOFC Anoden aufzuklären. Mittels elektrochemischer Impedanzspektroskopie wurden sowohl Grenzschichtkapazitäten als auch Polarisationswiderstände der Modellelektroden ermittelt. Der hauptsächliche Fokus der Arbeit war das Standardanodenmaterial YSZ/Ni.

Die kapazitiven Eigenschaften des YSZ/Ni Systems zeigten signifikante Abweichungen vom Stern-Doppelschichtmodell hinsichtlich des Absolutwertes der flächenspezifischen Kapazität und der Abhängigkeit der Kapazität von der Bias-Spannung und dem Wasserstoff-, Wasser- und Schwefelwasserstoffpartialdruck. Die Abweichungen konnten durch Annahme einer "chemischen" Kapazität (Batterietyp), bei der eine spannungsgetriebene Redoxreaktion einen Ladungsspeicher erzeugt, erklärt werden. Mehrere mögliche Mechanismen für eine solche chemische Kapazität im YSZ/Ni System wurden diskutiert.

Mittels Impedanzspektroskopie wurden elektrokatalytische Eigenschaften (Polarisationswiderstand) gemessen. Durch die Charakterisierung von Elektroden mit unterschiedlicher Dreiphasenlänge (aber gleicher Fläche) und Elektroden mit unterschiedlicher Fläche (aber gleicher Dreiphasenlänge) wurde der Ursprung der elektrochemischen Aktivität von YSZ/Ni bestimmt. Messungen an Elektroden mit unterschiedlicher Dreiphasenlänge ergaben, dass ein Teil der Aktivität von der Dreiphasengrenze stammt. Durch Messungen an Elektroden mit unterschiedlicher Fläche konnte zudem eindeutig gezeigt werden, dass ein signifikanter Teil der Wasserstoffoxidationsaktivität durch einen bisher unbekanntem flächenbezogenen Reaktionspfad verursacht wird. Variationen der Temperatur, des Wasserstoff- und Wasserpartialdruck und der Effekt von  $H_2S$  Zugabe konnten die Existenz des vorgeschlagenen Flächenpfad weiter verdeutlichen und chemisch charakterisieren. Mittels der erhobenen experimentellen Daten wurden zwei mögliche

Reaktionsmechanismen für den neu entdeckten Reaktionspfad diskutiert.

Um die Wissensbasis der Wasserstoffoxidationsmechanismen auf Metall/Keramik Elektrokatalysatoren zu erweitern, wurden die oben genannten Experimente auf YSZ/Ni auch auf folgende Materialkombinationen angewendet: YSZ/Pt, Scandium stabilisiertes Zirkonoxid/Ni und Titanoxid/Ni. Die Ergebnisse zeigten, dass sowohl das Metall, als auch die Keramikphase die elektrochemischen Eigenschaften beeinflussen und deshalb das Metall nicht schlicht als Stromsammler fungiert. Die Ergebnisse, zusammen mit Literaturdaten, zeigen weiters, dass die Aktivität von Modellelektroden entweder durch den Zustand der Elektrolytoberfläche oder durch Fremdphasen an der Dreiphasengrenze bestimmt wird.

# Contents

<b>1</b>	<b>Introduction</b>	<b>1</b>
1.1	Solid oxide fuel cells . . . . .	1
1.2	SOFC anodes . . . . .	4
1.3	Model anode literature review . . . . .	9
<b>2</b>	<b>Experimental</b>	<b>14</b>
2.1	General sample preparation . . . . .	14
2.2	Sample characterization . . . . .	20
2.2.1	Electrochemical evaluation . . . . .	20
2.2.2	Geometric evaluation . . . . .	21
2.3	Secondary ion mass spectrometry . . . . .	21
<b>3</b>	<b>Results &amp; Discussion</b>	<b>22</b>
3.1	Statistical criteria . . . . .	22
3.2	Nickel on yttria stabilized zirconia . . . . .	23
3.2.1	Sample characterization . . . . .	23
3.2.1.1	Geometric data . . . . .	23
3.2.1.2	Transmission electron microscopy . . . . .	24
3.2.1.3	Time of flight secondary ion spectrometry . . . . .	27
3.2.1.4	Electrochemical impedance spectroscopy . . . . .	29
3.2.1.5	Stability . . . . .	34

3.2.2	Capacitive behavior . . . . .	38
3.2.2.1	Influence of the area . . . . .	38
3.2.2.2	Influence of hydrogen sulfide . . . . .	40
3.2.2.3	Influence of bias and oxygen partial pressures	41
3.2.2.4	Covered electrodes . . . . .	42
3.2.2.5	Influence of temperature . . . . .	42
3.2.2.6	Discussion . . . . .	42
3.2.3	Electrocatalytic activity . . . . .	50
3.2.3.1	Influence of electrode geometry . . . . .	50
3.2.3.2	Influence of hydrogen sulfide . . . . .	51
3.2.3.3	Activation energy . . . . .	52
3.2.3.4	Influence of $H_2$ and $H_2O$ partial pressures . .	52
3.2.3.5	Discussion . . . . .	55
3.3	Variation of the metal and ceramic phase . . . . .	67
3.3.1	Platinum on yttria stabilized zirconia . . . . .	67
3.3.1.1	Reaction pathways . . . . .	67
3.3.1.2	Activation energy . . . . .	67
3.3.1.3	Influence of $H_2$ and $H_2O$ partial pressures . .	69
3.3.1.4	Discussion . . . . .	69
3.3.2	Nickel on scandia stabilized zirconia . . . . .	71
3.3.2.1	Reaction pathways . . . . .	71
3.3.2.2	Activation energy . . . . .	71
3.3.2.3	Influence of $H_2$ and $H_2O$ partial pressures . .	71
3.3.2.4	Discussion . . . . .	73
3.3.3	Nickel on titania . . . . .	74
3.3.3.1	Impedance spectrum . . . . .	74
3.3.3.2	Reaction pathways . . . . .	75



3.3.3.3	Activation energy . . . . .	76
3.3.3.4	Influence of $H_2$ and $H_2O$ partial pressures . .	77
3.3.3.5	Porous samples . . . . .	79
3.3.3.6	Discussion . . . . .	79
3.3.4	Metal-ceramic variation discussion . . . . .	82
<b>4</b>	<b>Conclusion</b>	<b>86</b>
	<b>List of Figures</b>	<b>91</b>
	<b>List of Tables</b>	<b>94</b>

# Chapter 1

## Introduction

### 1.1 Solid oxide fuel cells

In 2015 the world primary energy supply was 13.6 Gt o e (giga ton oil equivalent) with 81 % stemming from fossil fuel sources. [1] This energy consumption is furthermore expected to increase to 18 Gt o e or 17 Gt o e by 2035. [2] The significant utilization of fossil fuels as energy sources creates a two-fold problem: Firstly, fossil fuels are not renewable in an acceptable time-frame creating a limit on extractable energy from this fuel source. Secondly, carbon extracted from the lithosphere at a higher rate than returned to it accumulates in the atmosphere which intensifies the atmospheric greenhouse effect leading to higher global temperatures. It is therefore imperative to reduce the global consumption of fossil fuels, e.g. by increasing energy efficiency and increasing the amount of energy from renewable energy sources like solar, biofuel, and wind energy. One technology tapping into both methods of fossil fuel consumption reduction is the solid oxide fuel cell (SOFC), as it has higher energy conversion efficiency than traditional carnot-cycle based technologies (e.g. internal combustion engines) and is capable of utilizing many chemical fuel systems currently available. Additionally, lacking combustion

of fuel droplets and low operating temperatures (compared to internal combustion engines) harmful emissions like  $NO_x$ , particulate matter, and organic compounds are virtually absent. [3]

An SOFC, like other fuel cells, consists of 3 main components: The cathode (air electrode, oxygen is reduced), a dense electrolyte (ionically conducting, electronically blocking), and an anode (fuel electrode, fuel is oxidized). The specificum of an SOFC is that the electrolyte consists of a solid oxide ceramic which may facilitate proton or oxide ion conduction. (In the following only oxide ion conducting cells will be discussed) An exemplary scheme of an SOFC is shown in figure 1.1. Since significant oxide ion conduction in known materials only occurs at elevated temperatures, an SOFCs may be operated at temperatures ranging from 600 °C to 1000 °C. While at first glance this high operating temperature may seem to be a vice several advantages are linked to it: The use of a solid electrolyte gets rid of water management, high temperatures also eliminate the need of precious metals as electrode material, and internal reforming of organic fuels with usage of  $CO$  as fuel (counter to the PEMFC, which is deactivated by traces of  $CO$  [4]) makes a wide range of fuel sources possible. Of course, high temperatures also pose challenges like interconnect scaling (increased ohmic resistance/cell failure due to spallation [5]), grain coarsening in metal containing anodes (see below), stresses due to different thermal expansion coefficients, anode oxidation at shutdown, and potentially long startup times.

SOFCs may be classified by the single cell structurally supporting component (anode/electrolyte/cathode/interconnect/metal<sup>1</sup> supported[6]) and by the cell geometry in the stack (tubular/planar/integrated/segmented [6, 7]). The choice of the structurally supporting component comes with significant

---

<sup>1</sup>A porous metal substrate

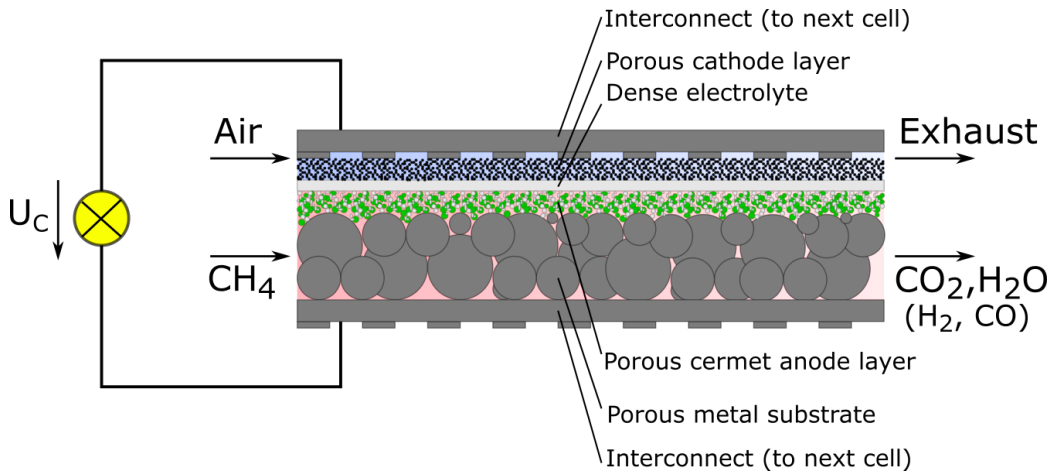


Figure 1.1: Schematic drawing of a planar metal supported solid oxide fuel cell fueled with methane. In an SOFC stack several cells are vertically connected which increases device voltage due to serial electrical connection.

implications for the overall system: In anode/electrolyte/cathode supported cells a ceramic is the structurally supporting material which can more easily lead to cell failure due to cracking<sup>2</sup>, while in interconnect and metal supported cells mechanical support is provided by a metal which greatly increases stability/ruggedness. [5, 6, 8] Additionally, anode supported cells (thick anode layer) are prone to cracking due to expansion of Ni in oxidizing conditions. [9] The mechanical disadvantages of anode supported SOFCs are, however, counteracted by the fact that the electrochemical degradation has been shown to be lower in anode supported cells compared to metal supported cells. [9] Several possible applications for SOFCs have been proposed and to varying degree realized. In the low-power segment (<1 kW) mobile battery charger units have been demonstrated [6], while in the medium-power segment (>1 kW, <100 kW) auxiliary power units for commercial vehicles have

<sup>2</sup>Of the 3 types the electrolyte supported cell has the best mechanical properties due to it being a dense layer

been demonstrated. [6] In high-power applications enough exergy flow is present in the exhaust gas that means to harness the high quality heat are worth the investment. One way to increase electrical efficiency is to feed exhaust fuel and air into a gas turbine. Further improvements to the design can be made by advanced cycle integration, e.g. by heat and steam recuperation [10]. Overall efficiencies of such power plants may be in excess of 60%. [11] Another possibility to improve overall efficiency is to integrate SOFCs (potentially with gas turbines) into combined heat and power systems (CHP, cogeneration), where exhaust heat is used to provide steam or hot water for heating (see Ref. [12] for a schematic). This concept of cogeneration can even be taken further in trigeneration plants, where not only electricity and heat are generated, but also refrigeration by an absorption cooler. In such a trigeneration plant it is possible to reach 80% overall efficiency. [13]

In general, the specifications for mobile applications, like the above mentioned battery charger and auxiliary power units, focus on fast startup times, resistance against mechanical stresses, redox stability and weight of the module. Due to the fragility of ceramic supported cells, metal supported cells are a natural choice in such applications. Stationary applications on the other hand require a long lifetime to recuperate initial investment while mechanical load is lower. Therefore, currently anode supported cells may be favored to metal supported cells in stationary applications due to the better long-term performance stability (see above).

## 1.2 SOFC anodes

While all areas of SOFC research have the potential of improving its capabilities and commercial potential, this thesis will focus on the electrochemical basics of the electrocatalysts. In FZ Jülich research on the cathode layer and

electrolyte for anode supported cells have yielded impressive improvements in cell performance over the last 25 years. [14] Metal supported cells on the other hand have by design less anode catalyst (typically a porous yttria stabilized zirconia (YSZ)/Ni cermet) in the cell which additionally has to be sintered in conditions unfavorable for the cermet anode microstructure.<sup>3</sup> These unfavorable anode conditions in metal supported cells, combined with the fact that most SOFC fuels contain sulfur impurities and carbon, warrant research into the improvement of anode performance. [15] Several factors besides simple electrochemical activity for fuel oxidation determine the usability of an anode in SOFC applications: [16]

- Reactant transport has to be given. This includes sufficient electronic and ionic conductivity in the anode layer and also fuel molecule transport to the electrochemically active sites.
- The thermal expansion coefficient should be compatible with other materials in the cell to prevent thermal stresses, especially during rapid startups.
- The anode materials should have high wettability with the electrolyte to stabilize the anode microstructure.
- Fuel flexibility should be made possible by the anode catalyst. This includes reforming activity to access hydrocarbons as fuel without pre-reformer.
- High tolerance to fuel impurities and carburization.
- Chemical stability of the anode in reducing and oxidizing conditions.

---

<sup>3</sup>Sintering steps have to be performed in reducing atmospheres to prevent substrate oxidation. Under these conditions only Ni metal is stable which sinters more easily than NiO.

- Material and processing cost should be low.

Obviously no known material/material combination fulfills all of the above mentioned criteria. The standard material currently used in SOFCs is a porous network of Ni and YSZ grains, commonly referred to as YSZ/Ni cermet electrodes. Besides being very active towards electro-oxidation of  $H_2$  and  $CO$  it is also a good catalyst for hydrocarbon reforming and chemically stable in reducing conditions. Ni not being a precious metal the material cost is relatively low and the manufacturing of the anode layer can be done without expensive vacuum methods by mixing NiO and YSZ powder with a binder and screen-printing the resulting ink. Additionally, the thermal expansion coefficient is better compatible with a YSZ electrolyte than Ni metal alone. [16] Disadvantages of YSZ/Ni cermet anodes, on the other hand, include the lacking redox stability, the high wetting angle between Ni and YSZ, the low melting point (1455 °C) of Ni<sup>4</sup>, and its sensitivity towards sulfur impurities in the fuel and carbon deposition.

Since SOFCs are generally expected to undergo several shutdowns and start-ups during their lifetime, the anode has to be able to survive these events with little damage. During shutdown oxygen from the cathode side can creep into the anode compartment through the electrolyte or imperfect seals which leads to oxidation of Ni in the YSZ/Ni network. This oxidation is accompanied by significant grain growth which can in the worst case cause cracks in the electrolyte layer. Upon reduction the Ni network seems to reorganize, resulting in a coarser network reducing its electrochemical performance and electrical conductivity. [16, 17] While a complete prevention of oxidation may be complicated or expensive to implement, a reduction of adverse ef-

---

<sup>4</sup>Leads to grain coarsening which reduces the electrochemically active reaction zone between Ni and YSZ.

fects on the cell may be reached by the use of YSZ powders with bimodal grain size distribution, anodes with higher porosity to accommodate grain growth, a lower Ni content (e.g. by lowering percolation threshold), and the use of graded anodes. [16]

Carbon deposition in anodes is a result of the use of carbon based fuels with a high C to O ratio, notably hydrocarbons. Carbon formation for hydrocarbons can proceed via the Boudouard-reaction ( $C + CO_2 \rightleftharpoons 2CO$ ), reduction of CO ( $CO + H_2 \rightleftharpoons C + H_2O$ ), or during the reforming process ( $C_nH_{2n+2} \rightleftharpoons nC + (n + 1)H_2$ ). [16, 18] The deposition of carbon leads to an envelopment of Ni particles which causes catalytic deactivation and can also lead to filament growth by dissolution-precipitation mechanisms. Accumulation of carbon obviously reduces open pore volume inhibiting fuel flow through the layer and can also lead to crack formation. [19] Since carbon deposition poses such a threat to SOFC operation, control of it is imperative. Using methane as a fuel, it is possible to prevent coking by lowering the operating temperature to kinetically inhibit carbon formation. It is also possible to increase current density to oxidize carbon before it accumulates, which enables higher operating temperatures. [20] When other fuels (e.g. diesel reformat) are employed, YSZ/Ni can still be used by adding steam (usually from the exhaust) to the fuel feed. This way the water gas shift reaction reduces the thermodynamical driving force for carbon formation, but due to the higher equilibrium oxygen partial pressure in the gas feed the efficiency decreases. To retain a higher efficiency, more coking resilient materials may be used; methods investigated in literature include alloying Ni with metals like Pt, Pd, Ru, and Cu or using Cu/gadolinium doped ceria (GDC) as an anode.[21]



Typical hydrocarbon fuels like natural gas, diesel, or biogas not only pose a carburization hazard to YSZ/Ni anodes, but usually also contain relevant amounts of sulfur impurities. Sulfur, in the form of  $H_2S$ , is a well-known catalyst poison for YSZ/Ni anodes and much research has been done on the characterization and mitigation of sulfur poisoning. [16, 21–36] In general, upon addition of  $H_2S$  in the ppm range the polarization resistance of a YSZ/Ni electrode increases very fast (within minutes) and then slowly keeps increasing during exposure. [28, 35, 37, 38] The operating temperature also affected the severity of sulfur poisoning with higher temperatures ( $>800^\circ\text{C}$ ) being associated with reversible and milder poisoning. [32, 35] It should be noted, however, that Deelebeeck et al. found that  $H_2S$  can act catalytic to hydrogen oxidation at temperatures below  $600^\circ\text{C}$ , which was explained by the formation of a thin  $Ni_2S_3$  film. [26] The current density of a cell has also been shown to influence sulfur poisoning. Analysis of seemingly conflicting results showed that increasing current density reduces the effect of  $H_2S$  exposure on the polarization resistance, as is expected since sulfur may be removed by oxidation at higher oxide ion flow. [23] Operation at higher current densities to mitigate sulfur poisoning, however, means operation of the cell in an undesirable low efficiency regime. Operational means of mitigating sulfur poisoning, i.e. higher temperatures and higher current densities, may not be acceptable choices for a given application. Hence, much effort has been devoted to alternative solutions - i.e. the search for more sulfur tolerant anode materials - to sulfur poisoning. Ref. [21] contains a comprehensive review on the sulfur tolerance of anode materials featuring 34 metallic elements. Interesting material systems proposed include alloyed YSZ/Ni, Ni/GDC[36], Cu/GDC/YSZ[39], and metal sulfides/thiospinells for operation in high concentrations of  $H_2S$ .

### 1.3 Model anode literature review

As shown above, significant efforts were devoted to improve the overall SOFC system in general and the anode in particular. While improvements in anode microstructure only need sparse input from the fuel conversion mechanism to maximize active sites in the anode, material selection/development can benefit from a more detailed understanding of the reaction mechanisms. Studies investigating the mechanism of fuel conversion reactions often benefit from systems as defined as possible, which makes the use of porous cermet electrodes problematic since the active zones are in general not accessible to analytic methods and transport reactions in the cermet (ionic, electronic, and gas diffusion) confound the desired electrocatalytic data. While modern FIB-SEM and X ray microtomography methods can reconstruct the geometry of cermets electrodes [40–42] these methods are not easily accessible and the definition of an electrode geometry is not possible due to the statistical nature of a cermet structure. Hence, geometrically simplified model systems, e.g. structured Ni thin films on YSZ (‘pattern electrodes’) or Ni wires pressed on a YSZ substrate (‘point electrodes’), were often used to investigate fuel conversion reaction (in the following if not otherwise noted hydrogen oxidation) mechanisms. In the following the current status of the field is summarized:

**Reaction pathway** Looking at the reactants in the hydrogen oxidation reaction, i.e.  $H_{2,g}$ ,  $H_2O_g$ ,  $O^{2-}$ , and  $e^-$ , it is chemically intuitive that each reactant is more or less confined to only one of the phases in the YSZ/Ni cermet electrode. For a reaction to occur all reactants have to meet in one place, which means the reaction has to take place at the triple phase boundary between metal, the electrolyte, and the gas phase. In 3D space this triple

phase boundary is a line and the catalytic activity may be modeled by the equations

$$R_{Pol} = R_{Pol,0} l_{TPB}^{-\alpha} \Leftrightarrow \quad (1.1)$$

$$\ln R_{Pol} = \ln R_{Pol,0} - \alpha \ln l_{TPB} \quad (1.2)$$

with  $R_{Pol}$  the polarization resistance,  $R_{Pol,0}$  the specific resistance,  $l_{TPB}$  the triple phase boundary length and  $\alpha$  an exponent which is 1 for an ideal triple phase boundary (TPB) active electrode. Experimentally the hypothesis of the TPB active electrode has been investigated by varying  $l_{TPB}$ , plotting it against the resulting polarization resistances in a double logarithmic diagram and fitting a line through the data. The resulting slopes are summarized in table 1.1. It can be seen that with a partial exception all values appear to be smaller than the ideal value of 1. This thesis will further investigate this apparent discrepancy of  $\alpha$  values to deepen the understanding of the reaction mechanism of hydrogen oxidation in YSZ/Ni electrodes.

**Impurities** One major difference from YSZ/Ni model electrodes to porous cermet electrodes is the surface-to-volume difference of Ni. In cermet electrodes particle sizes are typically in the  $\mu\text{m}$  or sub- $\mu\text{m}$  range, while thin film electrodes only have one dimension (thickness) in this size range. Significantly smaller surface-to-volume ratios are found for point electrodes (Ni wires pressed on YSZ), where the 2 small dimensions are in the range of  $500 \mu\text{m}$ . [43] The surface-to-volume ratio is the determining factor for how much impurities can segregate from the electrode bulk to the surface, hence structured thin film electrodes and especially point electrodes are more sensitive towards Ni bulk impurities than cermet electrodes are. Investigations of

point electrodes showed that for pure (99.995 %) and impure (99.8 %) Ni wires an impurity ridge forms at the TPB, although the size of the ridge is smaller with purer Ni.[43, 44] It has also been shown in these studies that pure Ni samples showed less polarization resistance than impure ones, although scattering between samples was significant. Secondary ion mass spectrometry (SIMS) analysis of the interface region (wires removed after measurement) showed that elements like Si, Na, K, and Al are depleted in the contact area between Ni and YSZ, while other elements like Mn and Ti are accumulated. [45] Analysis with higher spatial resolution further revealed a locally inhomogeneous distribution of impurities in the contact area. Investigations of Utz et al. [46] on pattern electrodes also showed some impurity features close to the TPB (striations, presumably due to electrode shrinkage) and at the YSZ/Ni interface ('grain imprint' along grain boundaries). SIMS measurements revealed that Na, K, Mg, Ca, Mn, and Ti are predominantly located at the YSZ surface, while Si and Al can be found mostly on the Ni electrode. The impurity feature size was 20 nm (Ni target purity in that study 99.98 %), which is similar to results in pure point electrodes. (Ref. [43]) Investigations of YSZ/Ni model electrodes should therefore be performed using very pure materials to reduce errors introduced by increased impurity segregation compared to cermet electrodes, although parity is hardly obtainable.

**Activation Energy** As shown in table 1.1 there doesn't seem to be good reproducibility between authors for activation energy values. Reported values range from 0.7 eV to 1.6 eV and different changes of activation energy with the temperature were reported: While Utz et al [47] reported a higher activation energy at lower temperatures, indicative of a co-limitation in series processes, Yao and Croiset [48] reported lower activation energies at lower temperatures, indicative of a co-limitation of parallel processes.

**$H_2/H_2O$  reaction order** Available data in literature (see table 1.1) suggest that hydrogen partial pressure has little to no influence on the polarization resistance of model Ni electrodes. Exponents scatter from -0.25 to +0.15 and most appear to be close to 0. For water, on the other hand, all authors agree on the activating nature of water and there seems to be a coalescence of reaction orders on two values: +1/3 and +2/3.

**Fuel** Besides pure hydrogen, also carbon monoxide was investigated as fuel gas on YSZ/Ni model electrodes. [49–51] Sukeshini et al [49] showed that the hydrogen oxidation reaction proceeds much faster than CO oxidation and that  $H_2$  oxidation was the dominant reaction in  $H_2/CO$  mixtures. Carbon deposition in  $CO/CO_2$  mixtures was also investigated showing that mainly graphitic and amorphous carbon are deposited on Ni, especially in electrolysis mode.[51]

**Capacitance** Several studies noted unusual capacitive behavior of YSZ/Ni electrodes. [43, 52–54] Absolute area specific capacitance (ASC) values exceeding conceivable values for Helmholtz double layer capacitances or higher than comparable systems were found by Primdahl et al. [52], Kek et al. [54], and Hansen et al. [43]. Additionally, dependency of the capacitance on water partial pressure [52] and overpotential [53] were found. For the system Au/YSZ Hendricks et al. developed a model based on the Gouy-Chapman theory with only one mobile ionic charge. [55] The model was capable of explaining the increasing ASC with the level of yttrium doping of zirconia and also explained a maximum of ASC at a certain electrode potential.

Study	Standard conditions		Parameters				$\alpha$
	T °C	$p_{H_2}$ , $p_{H_2O}$ kPa, kPa	Ea eV	RO $H_2$	RO $H_2O$		
Mizusaki et al [56]	700	1.01, 0.85	-	$\sim 0^a$	0.86 (850 °C)	/ <sup>b</sup>	
Mizusaki et al [57]	700	- <sup>c</sup>	-	$\sim 0$	not linear	-	
De Boer [58]	850	98, 2.3	1.61	-0.25	0.35( $p_{H_2}$ = 81 kPa)	-	
Bieberle, Gaukler [59]	700	25,1,2	-	-	-	0.8±0.04	
Bieberle et al [53]	700	15, 0.01	0.88	0.11 <sup>e</sup>	0.67 <sup>d</sup>	0.67/1.2	
Rao et al [60]	-	99, 1	1.02/0.74( $p_{H_2O}$ = 3 kPa) <sup>e</sup>	-	-	-	
Bessler/Utz et al [47, 61]	800	84, 17	1.01(800 °C to 700 °C)/ 1.37(650 °C to 450 °C)	-0.13( $p_{H_2O}$ = 0.69 kPa)/ 0.08( $p_{H_2O}$ = 6.4 kPa) <sup>f</sup>	0.69( $p_{H_2}$ = 9.2 kPa)/ 0.60( $p_{H_2}$ = 46 kPa)	-	
Yao, Croiset [48]	700	50, 3	0.73(500 °C to 600 °C)/ 1.17(650 °C to 800 °C)	0.092-0.145	0.3(550 °C, $p_{H_2}$ = 20 kPa)	0.7/0.72(750 °C)	

*Table 1.1: Summary of literature results for YSZ/Ni model electrodes, including activation energies, hydrogen and water reaction orders, and the  $l_{TPB}$  scaling exponent  $\alpha$ . Standard conditions apply if not otherwise noted in the property or variation is necessary to measure the property.*

<sup>a</sup>At 850 °C and low  $p_{H_2}$  0.5

<sup>b</sup>Linear relationship between conductance and  $l_{TPB}$ .

<sup>c</sup>Higher with increasing overpotential

<sup>d</sup>1/3 at higher overpotentials.

<sup>e</sup>1.02 eV on a YSZ single crystal, 0.74 eV on a YSZ polycrystal.

<sup>f</sup>Values from -0.15 to 0.14 measured.

# Chapter 2

## Experimental

### 2.1 General sample preparation

Samples measured in this thesis consist of the following layers (from bottom to top):

1. A porous YSZ/Ni cermet counter electrode layer
2. A 10 mm × 10 mm × 0.5 mm (111) YSZ single crystal
3. A ceramic thin film layer (optional)
4. A sputter deposited metal layer
5. A YSZ top-layer grown by pulsed laser deposition (PLD) (optional)

A schematic sample processing procedure is shown in figure 2.1, materials and equipment used for sample production and characterization are summarized in tables 2.1 and 2.2. The counter electrode was applied by screen-printing one layer of NiO/YSZ paste and one layer of Ni contacting paste on the unpolished side of the YSZ crystal. The dried layers were then sintered for 2 h at 1250 °C in air.

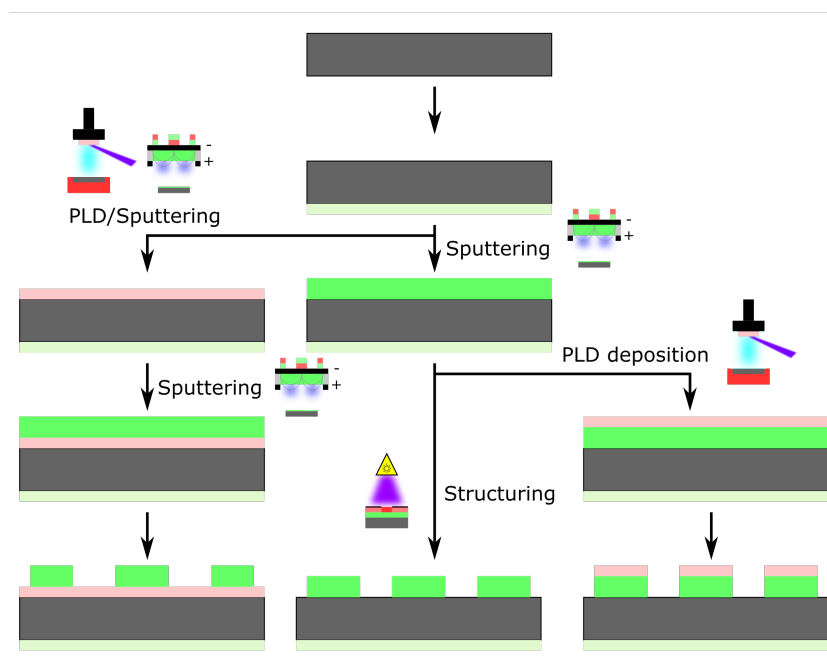


Figure 2.1: General sample preparation workflow. Green layers represent a metallic layer, pink layers a ceramic layer.



The optional ceramic layer on the YSZ substrate was prepared by either PLD or magnetron sputter deposition on the polished side of the crystal (with counter electrode). In case of PLD the deposition was conducted at 650 °C in  $4 \times 10^{-2}$  mbar O<sub>2</sub>. The laser energy per pulse was 400 mJ with a pulse frequency of 5 Hz. The target-substrate distance was set to 6 cm and the cooling rate after deposition was 15 K min<sup>-1</sup>. In case of sputter deposition the metal target (Ti) was deposited at an Ar pressure of  $7 \times 10^{-3}$  mbar and a current of 100 mA which resulted in a deposition rate of 0.07 nm s<sup>-1</sup>. To ensure a stable oxidic layer the sputter deposited layer was equilibrated at 800 °C in air.

The metal layer was deposited using magnetron sputtering. The deposition of Ni was conducted at an Ar pressure of  $8 \times 10^{-3}$  mbar and a current of 150 mA which resulted in a deposition rate of 1 nm s<sup>-1</sup>. The targeted thickness for Ni layers was 1200 nm. For Pt layers 400 nm were deposited at  $2 \times 10^{-2}$  mbar Ar and a current of 100 mA (deposition rate of 0.7 nm s<sup>-1</sup>). After deposition the metallic thin films were recrystallized for 5 h at 800 °C in 2.5 kPa H<sub>2</sub>/0.15 kPa H<sub>2</sub>O/balance Ar.

If a ceramic top-layer on the (recrystallized) metal layer was designated for the sample, this layer was deposited via PLD. Besides the atmosphere of  $4 \times 10^{-2}$  mbar 2.5 % H<sub>2</sub>/balance Ar to prevent scaling of the Ni thin film the deposition parameters were the same as described above.

Structuring of films was performed using photolithography. First, a layer of photoresist was spincoated for 30 s at 150 Hz and baked for 120 s at 100 °C. Afterwards, the sample was selectively illuminated with a UV-lamp for 40 s using a mask and developed until only the desired structures were covered by photoresist. The final etching step depended on the sample type: While samples with a Ni top layer were chemically etched in aqua regia, Pt thin films

were etched using Ar ion beam etching (3 kV, about 2 mA,  $1.1 \times 10^{-4}$  mbar Ar). In case of a ceramic top layer on the Ni film, ion etching was done to remove the ceramic layer, followed by etching in aqua regia. Afterwards, the sample was washed in water and the photoresist was removed in ethanol. More specific, the following sample types were prepared in this thesis (counter electrode preparation is the same for all):

- YSZ/Ni: After counter electrode preparation 1200 nm of Ni were sputter deposited and structured using chemical etching.
- YSZ/Ni/YSZ: After counter electrode preparation 1200 nm of Ni were sputter deposited and on top of the Ni layer 30 nm of YSZ were deposited via PLD (reducing atmosphere). The layers were structured by first ion etching the YSZ layer and then chemically etching the Ni layer.
- YSZ/Pt: After counter electrode preparation 400 nm of Pt were sputter deposited and the layer structured via ion etching.
- YSZ/SSZ/Ni: After counter electrode preparation 60 nm of scandia stabilized zirconia (SSZ) were deposited via PLD (oxidizing conditions). On top of the SSZ layer a Ni layer was deposited and structured analogously to YSZ/Ni samples.
- YSZ/TiO<sub>2</sub>/Ni: After counter electrode preparation 30 nm of TiO<sub>2</sub> were sputter deposited (Ti target) and the layer equilibrated at 800 °C in air for 3 h. Afterwards a Ni layer was deposited and structured analogously to YSZ/Ni Samples. Optionally, the structured sample was ion etched to remove the parts of TiO<sub>2</sub> not covered by Ni.

Table 2.1: Material list.

Material	Description
(111)YSZ substrate	$ZrO_2 : Y(111)K$ (9.5 mol% $Y_2O_3$ ) single sided epi-polished, 10 mm $\times$ 10 mm $\times$ 0.5 mm (Crystec, GER)
NiO/YSZ paste	1 g of NiO/YSZ powder (Fuel cell materials, USA) mixed with 0.25 g of ink vehicle (Fuel cell materials, USA)
Ni contacting paste	1 g of a 10 % ethyl cellulose/90 % Mond-Ni mixture mixed with 0.40 g of ink vehicle (Fuel cell materials, USA)
Ni sputter target	0.125 mm thick Ni foil, 99.99 % purity (Advent RM, UK)
Pt sputter target	99.95 %
Ti sputter target	BAL-TEC, LIE
YSZ powder (PLD target)	TZ-8Y (TOSOH, JAP)
SSZ PLD target	Treibacher, AT
Photoresist	ma-N 1420 Negativ Photoresist (Micro Resist Technology GmbH, GER)
Developer	ma-D 533S Developer for Photoresis (Micro Resist Technology GmbH, GER)
ARCAL	2.4 % $H_2$ in Ar (Air Liquide, AT)
$H_2S$ -ARCAL	209.5 ppm $H_2S$ , 2.5 % $H_2$ in Ar (Air Liquide, AT)
Hydrogen gas	99.999 %, Air Liquide, AT
Porous sample	Symmetrical layers on a thin YSZ support provided by Plansee SE

Table 2.2: Equipment list.

Device	Description
Sinter furnace	CWF1300 (Carbolite, GER)
Screen printer	Manual screen printer (Putz GmbH, AT)
Sputter machine	MED020 Coating system, QSG100 Quartz Film Thickness Monitor (BAL-TEC, now Leica Microsystems, AT)
Spin coater	Delta6RCTT (SUSS MicroTec, GER)
UV lamp	350W high pressure <i>Hg</i> lamp, maximum intensity 365nm (Ushio Inc., JAP)
Lithography masks	Quartz glass plate with structured Cr layer (Rose Fotomasken, GER)
Ion etcher	Plasma source: TPIS Plasma Source (tec tra, GER)
PLD	Laser: Compex Pro 201F KrF Excimer laser
Impedance spectroscopy device	Alpha-A High Performance Frequency Analyzer & Electrochemical Test Station POT/GAL 30V/2A (Novocontrol Technologies, GER)
Furnace (Micro-Macro setup)	SR 70-200/12SO (Gero GmbH, GER)
Optical Microscope	Axio Imager M1m (Zeiss, GER)
SEM	Quanta 200 FEG (FEI, USA)
TEM	FEI Tecnai F20 (FEI, USA)
SIMS	ToF-SIMS 5 (ION-TOF GmbH, GER)

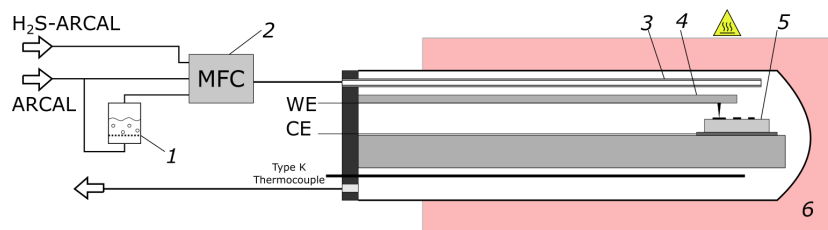


Figure 2.2: Sketch of the electrochemical measurement reactor. 1 humidifier, 2 mass flow controller, 3 gas piping in the reactor, 4 movable WE contacting cantilever with contacting needle, 5 sample, 6 furnace.

## 2.2 Sample characterization

### 2.2.1 Electrochemical evaluation

Electrochemical measurements were conducted in a setup which allows controlling gas atmosphere, composition, and temperature and offers the possibility to contact individual electrodes on a sample. The setup used is sketched in figure 2.2. The sample is placed into a sealed flow reactor inside a furnace, where the counter electrode is contacted with a Pt sheet and the working electrodes are contacted using Ni needles (unless otherwise noted) attached to movable cantilevers. To increase statistics, the setup used 4 cantilevers to measure 4 electrodes in one run and the electrodes were measured sequentially using a demultiplexer switch box. If not otherwise noted, only alumina, Pt, Ni and the sample are present in the hot zone of the setup to prevent deposition of foreign phases on the sample. (Type K thermocouple was shielded with a closed alumina pipe)

Electrical characterization was conducted using electrochemical impedance spectroscopy in a 2-point setup. Data obtained from the analyzer were evaluated using CNLS-fitting provided by the software ZView 3.1 (Scribner Associates, Inc.).

### 2.2.2 Geometric evaluation

The geometric properties of measured electrodes were evaluated individually for each electrode using optical microscopy in transmitted light dark field mode. The images were then processed using a custom semi-automatic image processing tool in the microscope software package AxioVision 4.8.2.0 (Zeiss, GER).

## 2.3 Secondary ion mass spectrometry

Time of Flight Secondary Ion Mass Spectrometry was measured on a ToF-SIMS 5 instrument using  $Bi^+$  ions in the high current bunched mode. For the primary beam a  $Bi^+$  beam with the energy 25 keV, a field of view of  $500\ \mu\text{m} \times 500\ \mu\text{m}$ , and a resolution of 512x512 was used. For the  $O_2^+$  sputter gun 600 nA at 2 keV and a crater size of  $800\ \mu\text{m} \times 800\ \mu\text{m}$  were used. Charge compensation was provided by low energy electrons (20 eV).

# Chapter 3

## Results & Discussion

### 3.1 Statistical criteria

The statistical significance for this thesis is defined as  $\alpha = 0.05$ . This significance indicates that in statistical tests a true null-hypothesis will be rejected only in 5% of decisions (Type I error, ‘false positive’). For the most often used statistical test in the thesis (the 2-sample *t*-test for equal means) this significance implies that a difference in mean values is erroneously concluded in maximally 5% of decisions. The reader should note that statistical significance does not yield information about Type II errors (‘false negative’), where the null hypothesis is erroneously accepted.

## 3.2 Nickel on yttria stabilized zirconia

### 3.2.1 Sample characterization

#### 3.2.1.1 Geometric data

Micro-patterned thin-film electrodes have, compared to porous cermet electrodes, the advantage of being geometrically well-defined. The desired geometry is produced in the structuring step and defined by the lithographic mask. While closely linked, the resulting electrode geometry does not exactly match to the (known) mask geometry. This is due to the etching step in which grains are etched with different speed, leading to a corrugated edge and a certain undercut in the photoresist reducing the size of the structures. Additionally, defects in the photoresist layer can lead to holes in the electrode. In order to draw more reliable conclusions based on geometric parameters every electrode was geometrically characterized before measurement.

This characterization was performed using transmitted light optical microscopy. Due to strong light scattering and absorption of the counter electrode dark field mode was used and stray light reduced by placing the sample in a light blocking sampleholder. Acquired images were then evaluated by a semi-automatic custom program to obtain the area and circumference ( $l_{TPB}$ ) of the electrode.

Since the target geometry of electrodes is not met exactly, a closer analysis of aggregated geometric data is warranted. For the electrode series with varying  $l_{TPB}$ , but nominally constant area and the series with varying area, but nominally constant  $l_{TPB}$  the two geometric properties are plotted against each other in figure 3.1. For the series with nominally constant area it can be seen that for a change in  $l_{TPB}$  by a factor of 23 a change in projected



area by a factor of maximally 2 follows.<sup>1</sup> Hence, the assumption of constant area is valid in cases where the TPB effects are dominant. Analogously, for the electrode series with nominally constant  $l_{TPB}$  the area changes by a factor of 6.4 (geometry series 2)/21 (geometry series 3) while the  $l_{TPB}$  changes by a factor of 1.12 (geometry series 2)/1.15 (geometry series 3). This electrode series is thereby remarkably close to the intended geometry and will therefore be used to more precisely separate area- and TPB-effects. The average  $l_{TPB}$  of the geometry series 3 is 4.03 mm, which will be used for geometric normalization in the subsequent sections.

As geometrically defined electrodes are crucial for the interpretation of data in this thesis, higher resolution images of a typical YSZ/Ni sample were acquired using scanning electron microscopy (SEM). The images are shown in figure 3.2. The figure shows that even in higher resolutions no small scale pores are visible and that the TPB appears smooth. It can therefore be concluded that the  $l_{TPB}$  obtained by optical microscopy corresponds to the real  $l_{TPB}$  of the electrode. Additionally, the surface of the Ni electrode is covered with particles on some samples. While the origin of the particles is unknown, it is possible that these particles are remnants from the Ni recrystallization phase of the preparation or impurity particles.

### 3.2.1.2 Transmission electron microscopy

From typical sample electrodes lamella were cut using focused ion beam, placed on a TEM sample holder and characterized in a transmission electron microscopy (TEM). A low-magnification dark field image of the lamella can be seen in figure 3.3. The image shows that on top of the flat zirconia substrate large Ni grains (about 2  $\mu\text{m}$ ) constitute the Ni layer without gaps

---

<sup>1</sup>The change in Ni surface area is less pronounced as the ideal total surface area is the projected area plus  $l_{TPB}$  times thickness

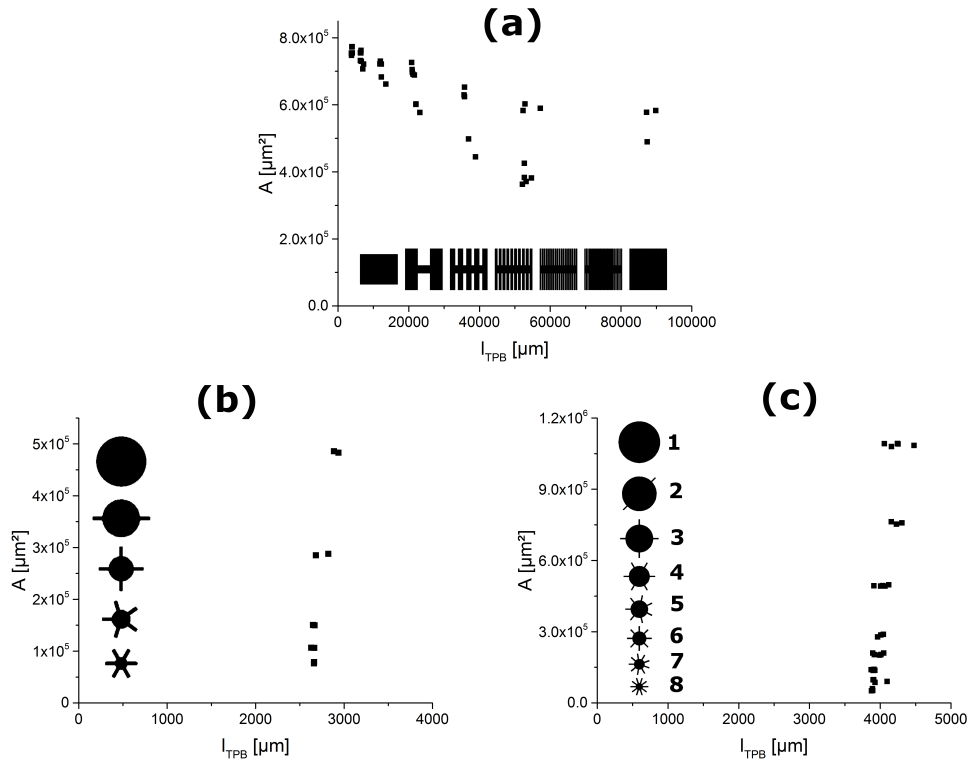


Figure 3.1:  $l_{TPB}$  vs. area plots for different electrode geometries used in this thesis. Inserts show a sketch of the electrode geometry. (a) Geometry series 1: Electrodes with nominally constant area. (b) Geometry series 2: Electrodes with nominally constant  $l_{TPB}$  used for capacitive measurements. (c) Geometry series 3: Electrodes with nominally constant  $l_{TPB}$  used for resistive measurements.

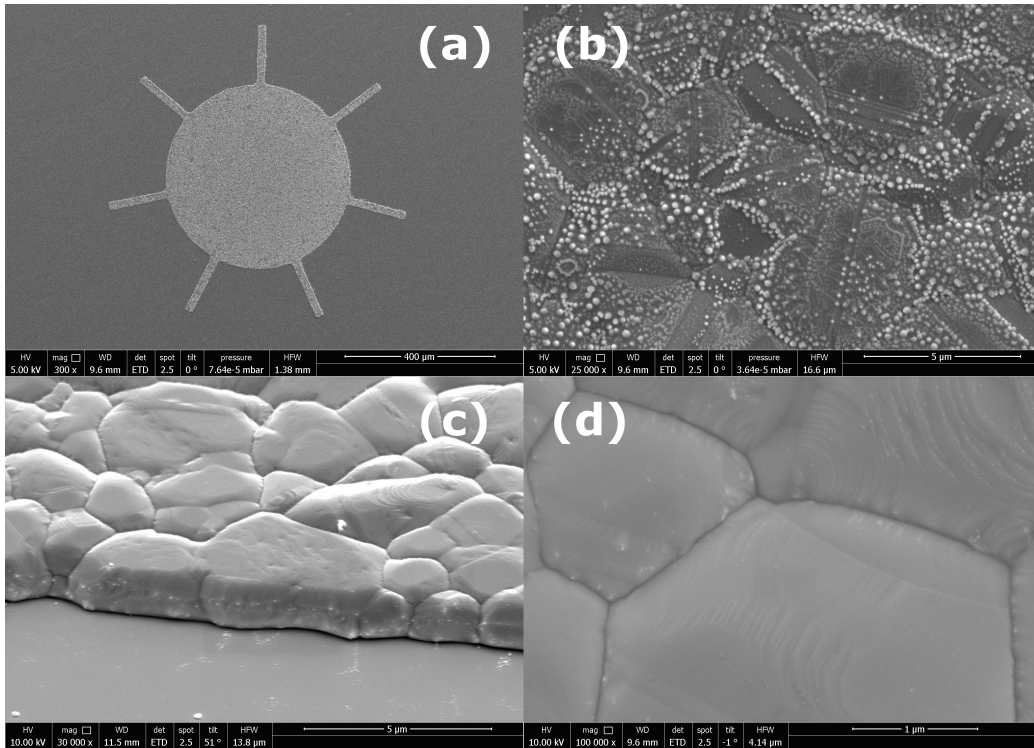


Figure 3.2: SEM images of YSZ/Ni electrodes. (a) Low magnification of an electrode of the size 5 (see figure 3.1c). (b) Zoom on the Ni electrode from (a). (c) Tilted image of the TPB region. (different sample) (d) High magnification image of Ni surface. (electrode from (c))

between them. Looking at the interface, EDS analysis shows no signs of interdiffusion of Ni and Zr or Y (see figure 3.4) and also no indications for the presence of Si (see figure 3.5). It should, however, be noted that for very thin layers the detection limit for Si might not be reached. High resolution TEM images of the interface and the TPB region are shown in figure 3.6. It can be seen that at the interface far from the TPB an interlayer of about 1 nm could be found, which, judging by visible ion size, is probably oxidic. At the TPB the interlayer has a thickness of about 3 nm and EDS analysis (see figure 3.5) of this region shows a weak Si signal.<sup>2</sup> From the above mentioned observations it can be concluded that at the interface between the dense Ni film and YSZ some interlayer with unknown composition exists. This layer may be (partly) due to natural YSZ yttria segregation at the (sub)-surface [62], or caused by impurity segregation.

### 3.2.1.3 Time of flight secondary ion spectrometry

To investigate the chemical composition of the surface region of the Ni electrode and the electrolyte a SIMS measurement was conducted on a sample after electrochemical experiments. The resulting lateral profile of various ions is shown in figure 3.7. The figure shows the summed intensities of 230 xy-scans with 1 s sputtering of the  $O_2^+$  gun in between scans. The figure shows that the main impurities found are Si, Na, and K, which are predominantly located on top of the Ni electrode. Minor impurities, like Mg, Ca, and Cr can be found on the YSZ surface. These results are, besides the alkali metals, in agreement with literature. (see section 1.3)

---

<sup>2</sup>It should be noted that Si presence could not be corroborated in EELS analysis of the TPB region.

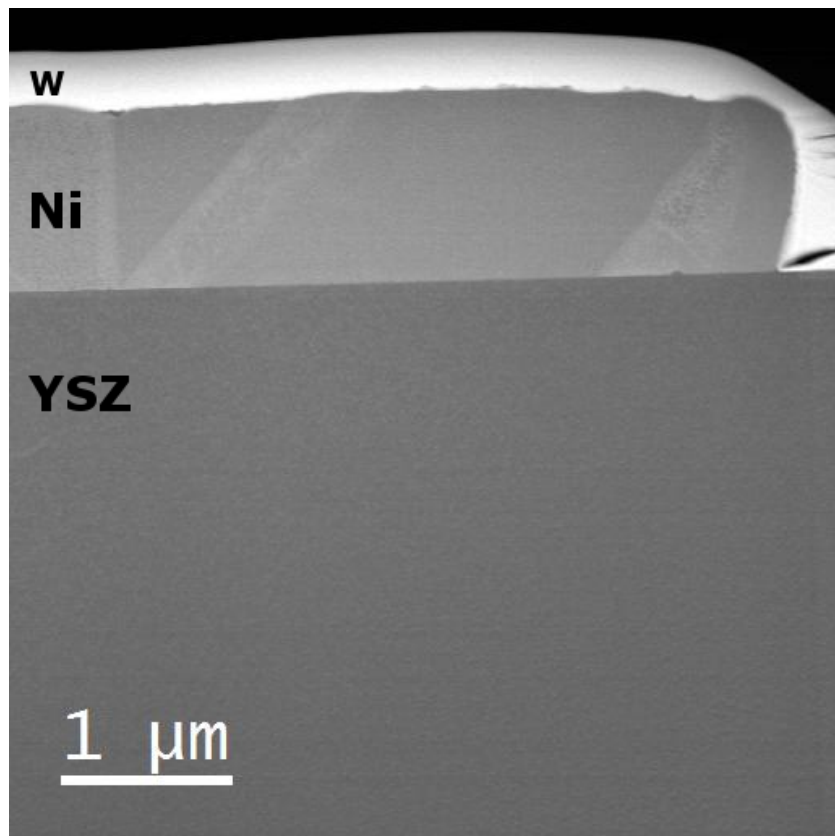


*Figure 3.3: STEM-HAADF image of a YSZ/Ni FIB-lamella.*

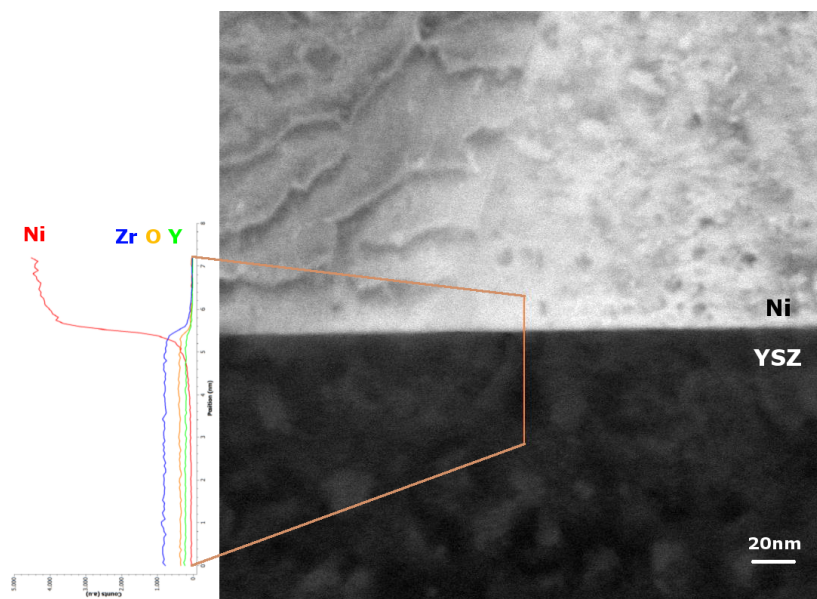


Figure 3.4: STEM-HAADF image of the YSZ/Ni interface. Left side: Line scan EDS signals for Ni, Zr, Y and O.

### 3.2.1.4 Electrochemical impedance spectroscopy

Impedance spectra were recorded with a  $10 \text{ mV}_{RMS}$  stimulus to ensure linearity of the voltage-current curve in the relevant voltage range. A typical impedance spectrum of a YSZ/Ni sample is shown in figure 3.8. It can be seen that the spectrum consist mainly of a slightly asymmetric and depressed semicircle feature and a small  $Z_{Re}$  high frequency intercept in the Nyquist-plot. Such a spectrum was therefore fitted using a resistor||constant phase element (CPE) circuit with a series resistor element as shown as insert in figure 3.8. Since the asymmetry may distort resistive data, two fitting strategies were employed:

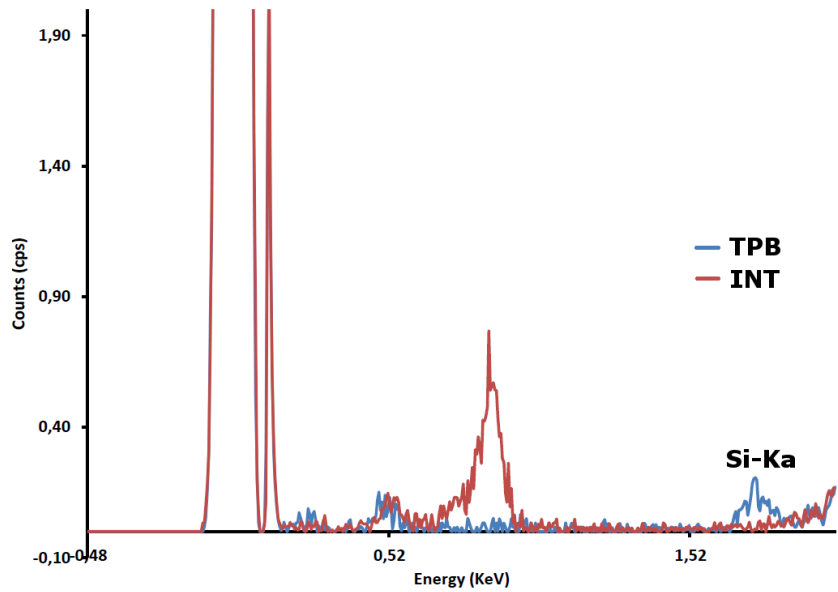
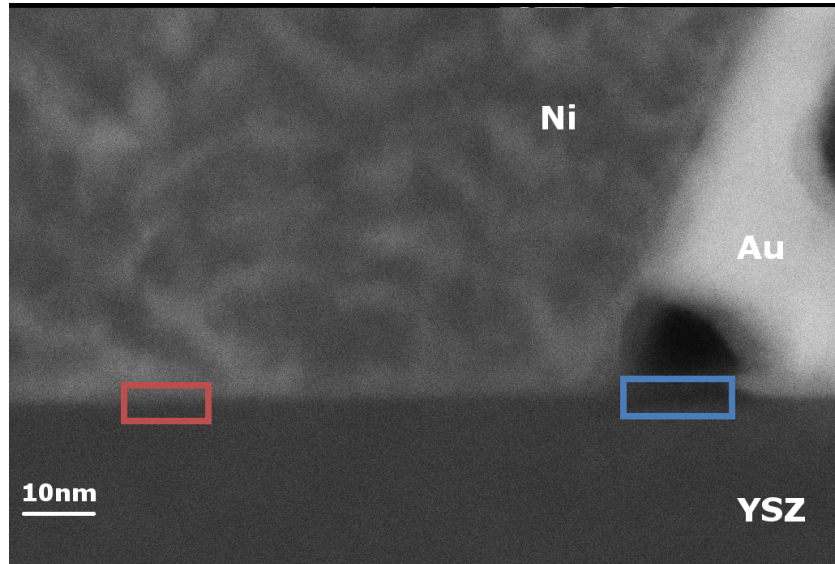


Figure 3.5: Top: STEM-HAADF image of the YSZ/Ni interface and TPB region. The Au layer is a protective FIB layer. Bottom: EDS spectra for the interface region (red rectangle in top image) and the TPB region (blue rectangle). Si could only be detected for the TPB region.

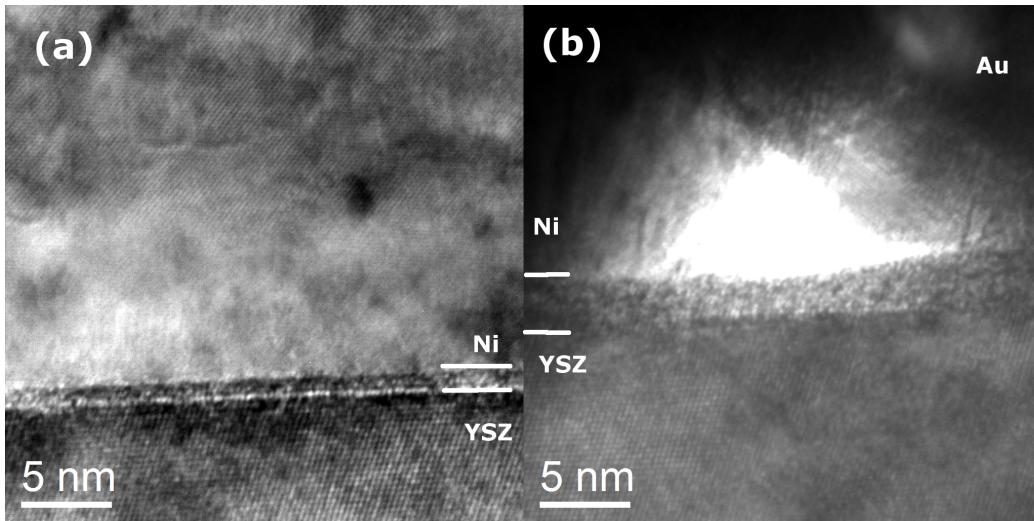


Figure 3.6: High resolution TEM images of (a) the YSZ/Ni interface and (b) the TPB region. Interlayer boundaries between Ni and YSZ are marked with white lines. The Au layer is a protective FIB layer.

1. For capacitive data analysis the whole spectrum from 1 MHz to 5 mHz was fitted. An example fit is shown in figure 3.8. (denoted as ‘capacitance fit’)
2. For resistive data analysis first the whole spectrum was fitted as above. After fixing the series resistance from the previous fit, the spectrum was fitted in the frequency range of 1 Hz to 5 mHz. This way a more precise fit for lower frequencies and therefore a more precise DC resistance is obtained. An example fit is shown in figure 3.8. (denoted as ‘resistance fit’)

These fitting strategies obviously only constitute an approximation for the fundamental, more complex processes behind this AC current behavior. This equivalent circuit assumes only one distinct relaxation time, however, in actuality a distribution of thereof would be more accurate. Since a detailed and



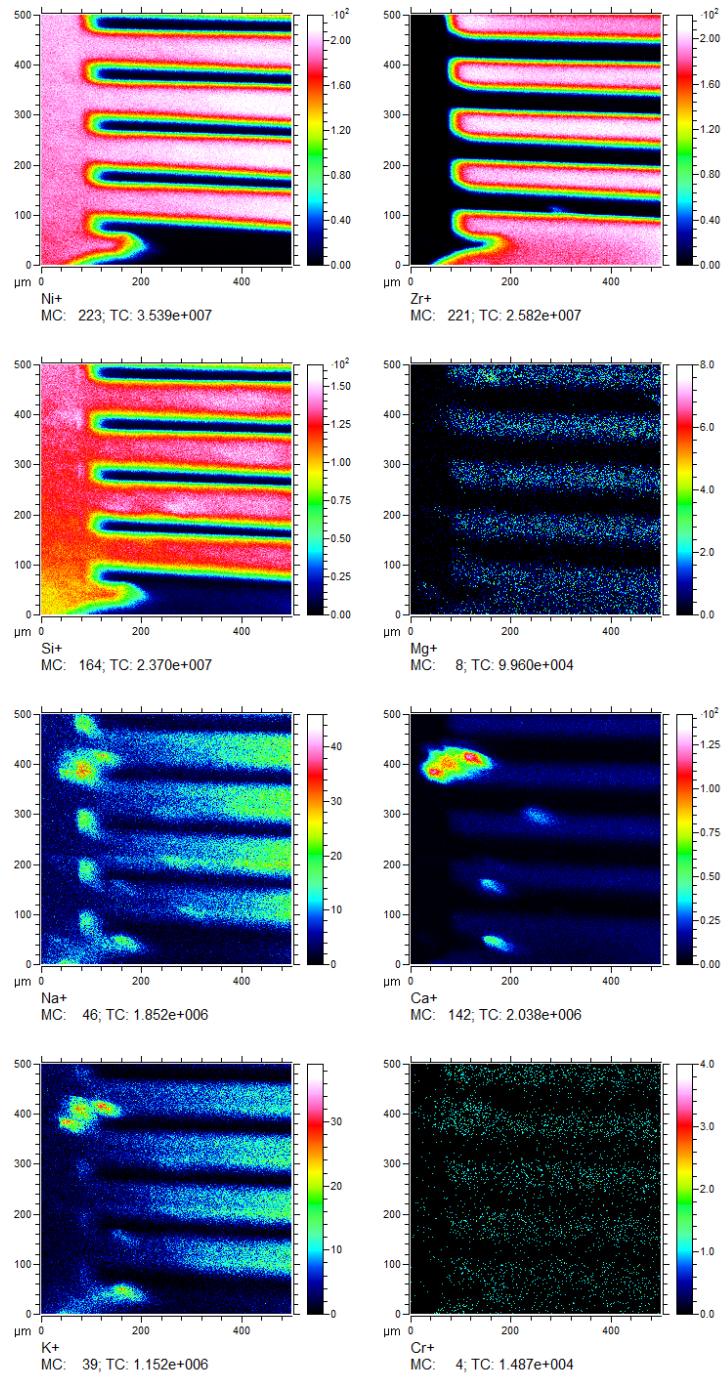


Figure 3.7: Lateral ToF-SIMS ion profile of a typical YSZ/Ni electrode after measurement. Besides Ni and Zr (to mark the electrode and free YSZ surface) common impurity ions are shown.

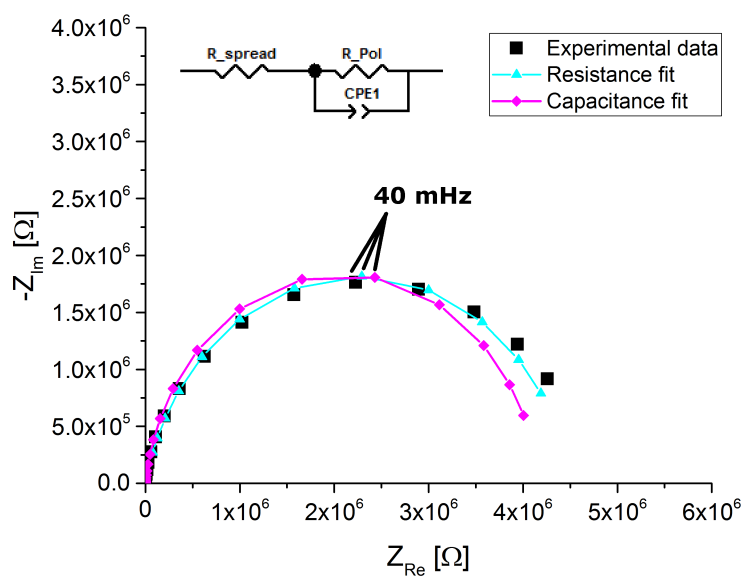


Figure 3.8: Typical Nyquist plot of a YSZ/Ni impedance spectrum with the two types of fits used in this study. For the capacitance fit the whole frequency range (1 MHz to 5 mHz) was fitted, while for the resistance fit the frequency range of 1 Hz to 5 mHz with fixed high frequency  $Z_{Re}$  was used. Insert shows the equivalent circuit used for fitting. Conditions: 800 °C, 2.5 kPa  $H_2$ /0.15 kPa  $H_2O$ /balance Ar.

quantitative mechanistic description of the impedance spectrum is beyond the scope of this thesis only the following ‘system macroscopic’ quantities will be extracted and interpreted from the spectra:

1. In analogy to previous work on Pt/YSZ electrodes, the high frequency series resistance is interpreted as the spreading resistance of ion transport of the electrolyte. [63] (with an additional small resistive contribution of the wiring, about  $5\ \Omega$ )
2. The resistance of the main feature in the Nyquist-plot is interpreted as the polarization resistance of the electrochemical reaction at the YSZ/Ni electrode.
3. The capacitance of the YSZ/Ni electrode is extracted from R||CPE data. The impedance of a general CPE is given by  $Z_{CPE} = \frac{1}{T(i\omega)^P}$  with  $\omega$  the angular frequency and  $T$  and  $P$  as CPE parameters. For the special case of  $P = 1$  the impedance of a CPE is identical to the impedance of a capacitor. Since  $P$  values in YSZ/Ni spectra are around 0.9 and therefore close to 1, this CPE can be interpreted as a non-ideal capacitor. Capacitance values were obtained by calculating the peak frequency  $\omega_P$  of the R||CPE sub-circuit and from this peak frequency calculating the equivalent capacitance in the corresponding R||C sub-circuit according to  $\omega_P = 1/RC$ . [64]

### 3.2.1.5 Stability

Exposure of YSZ/Ni microelectrode to elevated water partial pressures has been shown to have a detrimental effect on the microstructure of electrodes, leading to pore formation. [65] To investigate the temporal stability of YSZ/Ni microelectrodes used in this thesis, electrodes were held at standard

measurement conditions (800 °C, 2.5 kPa  $H_2$ /0.15 kPa  $H_2O$ /balance Ar) for 720 h. However, as figure 3.9a&b shows, no pore formation as described in the reference was observed for standard measurement conditions, even after long exposure. Additionally, hydrogen sulfide exposure may also influence the microstructure of the electrodes as liquid NiS can form at high concentrations. Figure 3.9c shows an electrode after exposure to 50 ppm of  $H_2S$  which displays no signs of structural change while figure 3.9d shows an electrode exposed to 100 ppm showing severe morphological changes of the electrode involving partial spherification to isolated Ni droplets. To ensure an intact microstructure, sulfur poisoning experiments were therefore limited to a maximum of 50 ppm of  $H_2S$ .

The temporal evolution of the polarization resistance and capacitance under standard operating conditions is shown in figure 3.10. Regarding the polarization resistance it can be seen that upon the first heating after about 1 Ms relatively stable values are obtained. After cooling down and reheating with the same electrodes contacted some further increase of the polarization resistance was observed. After cooling down and contacting differently sized electrodes (sizes 2/4/6/8 instead of 1/3/5/7 as before, see figure 3.1c) significantly different polarization resistance values were obtained, which also showed little to no degradation after an initial phase. In order to ensure comparable polarization resistance values between measurement runs, samples were therefore stabilized at measurement conditions for at least 1 Ms prior to contacting electrodes for the measurement run. Capacitance values on the other hand appear to be stable during the whole measurement cycle and no special pre-treatment was necessary to obtain values comparable between electrodes.

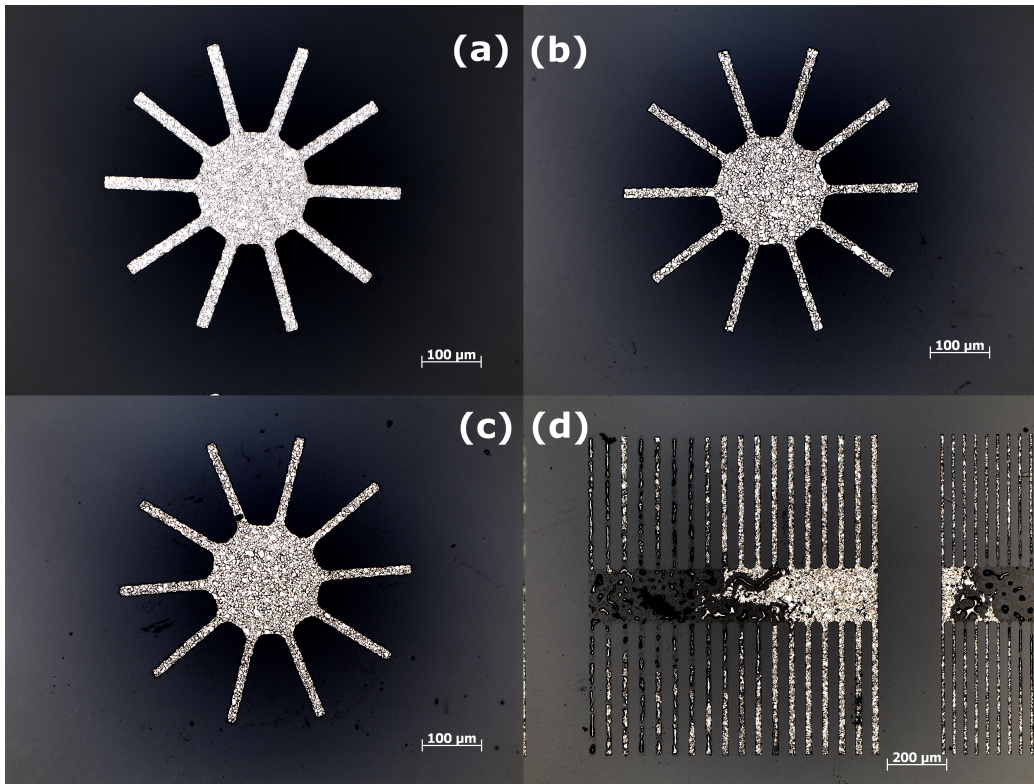


Figure 3.9: Ni microelectrode structure after different treatment. (a) After 10 h, (b) after 720 h at 800 °C, 2.5 kPa H<sub>2</sub>/0.15 kPa H<sub>2</sub>O/balance Ar. (c) Exposed to 5 Pa H<sub>2</sub>S/2.5 kPa H<sub>2</sub>/0.15 kPa H<sub>2</sub>O/balance Ar at 800 °C. (d) Exposed to 10 Pa H<sub>2</sub>S/2.5 kPa H<sub>2</sub>/0.15 kPa H<sub>2</sub>O/balance Ar at 800 °C.

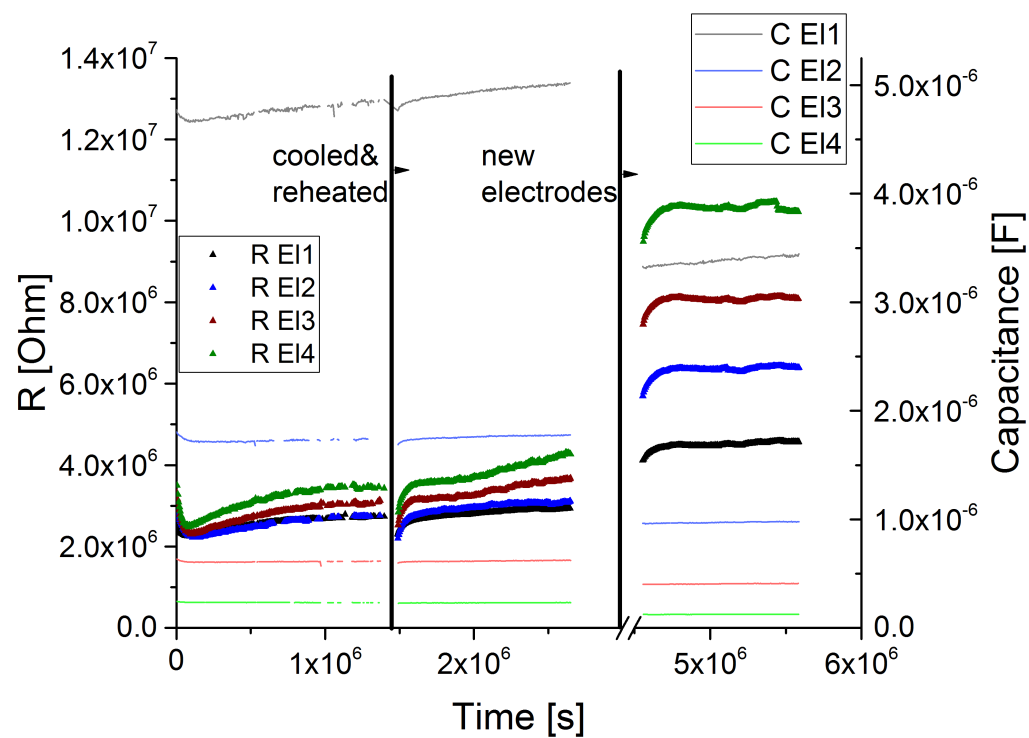


Figure 3.10: Temporal evolution of polarization resistances and capacitances during a long measurement run. Vertical lines indicate an intermission involving cooling down and reheating to measurement conditions. The second intermission was also used to contact different electrodes with the same nominal geometry on the same sample. Missing values are due to contacting issues. Conditions: 800 °C, 2.5 kPa H<sub>2</sub>/0.15 kPa H<sub>2</sub>O/balance Ar.

## 3.2.2 Capacitive behavior

The reader should note that a subset of data presented in this section has already been published in Ref. [66].

### 3.2.2.1 Influence of the area

Electrodes in aqueous electrochemistry as well as on solid electrolytes exhibit some capacitance originating at the interface between the electrode and the electrolyte. Since this interface spans a two dimensional plane a proportionality between the projected electrode area and the capacitance can be expected. Hence, electrodes of the geometry series 2 (area variation) were investigated for their capacitance (see section 3.2.1.4 for how the capacitance is calculated). Figure 3.11a shows the resulting capacitances as a function of the area when 2 different contacting needles were used, linear fitting results are shown in table 3.1. A t-test did not reveal a significant difference in slopes between the two samples (t-test assuming equal variance,  $p = 0.15$ ). As for the capacitance intercept confidence intervals of CI-95% [ $-7.9 \times 10^{-8}$  F,  $-2.3 \times 10^{-8}$  F] for the Ni needle and CI-95% [ $-8.6 \times 10^{-8}$  F,  $-4.6 \times 10^{-8}$  F] for the Pt needle were found. The intercept is therefore statistically significantly below 0. To investigate the effect of the electrode shape, also circular electrodes were measured, the results can be found in figure 3.11b. Again a very similar result can be found with an ASC of  $3.9 \text{ F m}^{-2}$  (different measurement conditions to above, see figure caption) and an intercept of  $-7.3 \times 10^{-8}$  F indicating no influence of the shape on the capacitance. The unexpected negative capacitance intercept points to some part of the area, potentially the needle contacted part, not participating in the capacitance forming process. A further investigation of this phenomenon is, however, beyond the scope of this thesis.

Table 3.1: Fitting results of area-capacitance diagrams shown in section 3.2.2.  $d$  denotes the capacitance-axis intercept, while  $k$  denotes the slope.  $R^2$  is shown as a measure of the fitting quality.

Description	$d$ [nF]	Std.err.	$k$ [ $\text{F m}^{-2}$ ]	Std.err.	$R^2$
Ni needle fig. 3.11a	-51	8.7	3.01	0.033	0.99952
Pt needle fig. 3.11a	-66	6.4	2.94	0.023	0.99973
Pre-S fig. 3.12	-40	24	2.99	0.086	0.99751
S exposed fig. 3.12	-45	8.0	2.57	0.028	0.99964
YSZ cover fig. 3.14	-80	23	2.92	0.079	0.9978

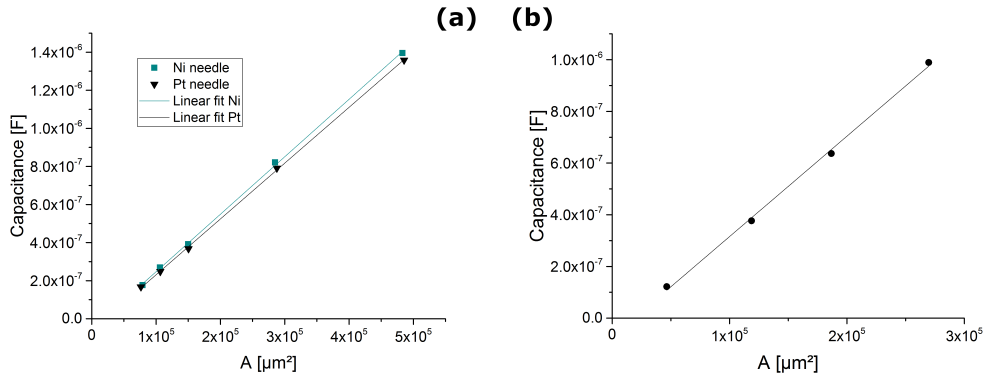


Figure 3.11: Effect of the geometry on the YSZ/Ni electrode capacitance. (a) Geometry series 2 with two different contacting needles. Conditions:  $800^\circ\text{C}$ ,  $2.5 \text{ kPa H}_2/0.15 \text{ kPa H}_2\text{O}/\text{balance Ar}$  (b) Circular electrodes of different sizes. Conditions:  $750^\circ\text{C}$ ,  $2.5 \text{ kPa H}_2/1.5 \text{ kPa H}_2\text{O}/\text{balance Ar}$ .



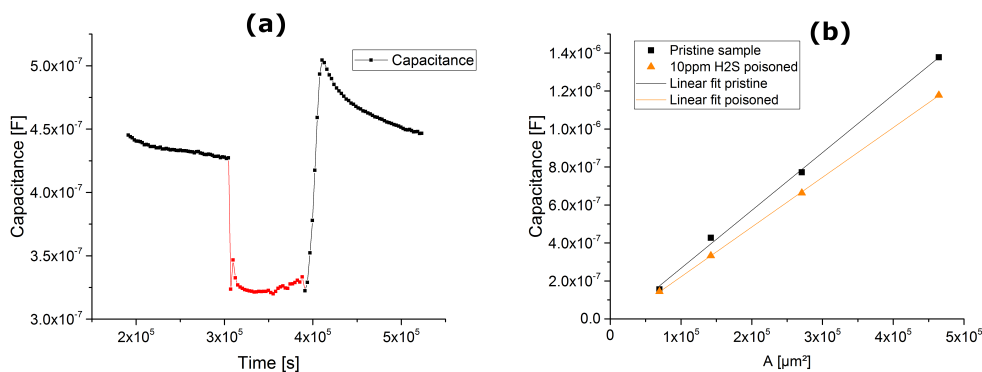


Figure 3.12: Influence of  $H_2S$  on the capacitance of YSZ/Ni electrodes. (a) Temporal development of the capacitance during a  $H_2S$  exposure experiment. Red points were measurements under the addition of 1 Pa of  $H_2S$  (b) Last capacitance obtained before/during exposure plotted as a function of the electrode area. Conditions:  $800^\circ\text{C}$ , 2.5 kPa  $H_2$ /0.15 kPa  $H_2O$ /balance Ar.

### 3.2.2.2 Influence of hydrogen sulfide

Electrodes of the geometry series 2 (area variation) were exposed to 10 ppm  $H_2S$  at measurement conditions to investigate the effect of chemical environmental change on the capacitance. Figure 3.12a shows the temporal progression of such an experiment. It can be seen that after addition of 10 ppm  $H_2S$  to the gas feed the capacitance ‘immediately’ (experimental time resolution of 25 min) decreases and increases again after removal of  $H_2S$ . Plotting the last pre-poisoned and the last poisoned capacitances against the area of the electrodes the plot in figure 3.12b is obtained. Linearly fitting the data series (for fitting data cf. table 3.1) it can be seen that the slopes - i.e. the ASC are statistically significantly different ( $p = 0.0097$ ). Hydrogen sulfide exposure therefore reduces the capacitance of YSZ/Ni electrodes.

### 3.2.2.3 Influence of bias and oxygen partial pressures

To investigate the influence of bias voltage on the capacitance of YSZ/Ni, electrodes of the geometry series 2 (area variation) were measured. Barring small low-frequency inductive loops in the Nyquist plot (not included in the fit) under high polarization, the shape of the impedance spectrum remained the same as in the unpolarized state. Figure 3.13a shows the capacitance of different electrodes in the same atmosphere as a function of the applied bias voltage. The general shape of the curves appears rather complex. On the highly cathodically polarized side a steep decrease of capacitance with bias voltage is observed. Under moderately cathodic polarization a minimum can be observed, while under anodic conditions the capacitance again slightly increases. Additionally, a hysteresis at polarizations between  $-150$  mV and  $100$  mV is observed. Moreover, this general shape of the curve is independent of the electrode size as several electrode sizes exhibit the same behavior.

Figure 3.13b shows that the above mentioned minimum seems to shift with the water partial pressure. This shift in minimum is approximately  $125$  mV, which is close to the Nernst voltage between the two atmospheres at  $800$  °C ( $120$  mV). Since this result suggests that the chemical potential of oxygen determines the behavior of the capacitance rather than the bias voltage, measurement atmospheres with different oxygen partial pressure were tested. For that, electrodes of the geometry series 3 (area variation) were measured in atmospheres with varying hydrogen or water partial pressure starting with a composition of  $2.5$  kPa  $H_2$ / $0.15$  kPa  $H_2O$ /balance Ar and then calculating the Nernst voltages to air using NIST data [67]. The resulting capacitances are plotted as a function of the nominal Nernst voltage of the respective gas composition to air - the obtained plot is shown in figure 3.13c. The figure shows that the general shape of the voltage-capacitance curve of the

bias variation can be reproduced by partial pressure variations. Moreover, plotting both bias voltage variation and atmosphere variation data in one diagram, as shown in figure 3.13d, the minima of all series appear to line up at around  $-1200$  mV (equivalent to a  $p_{O_2} = 6.0 \times 10^{-24}$  bar), which further shows that oxygen chemical potential is the property determining the bias voltage dependency of the YSZ/Ni capacitance.

#### 3.2.2.4 Covered electrodes

To investigate the effect of surface chemistry on the capacitance of YSZ/Ni electrodes the Ni layer was coated with 8YSZ prior to structuring (see section 2.1 for preparation). These ‘sandwich’ electrodes were then investigated analogously to the sections above (electrical contacting problems were not observed when contacting with Ni needles). The area *vs.* capacitance plot for such covered electrodes is shown in figure 3.14 with the fits being summarized in table 3.1. Comparing the fit of the covered electrodes and the pre-sulfur poisoning series fit no significant difference in slope could be found ( $p = 0.59$ ). The apparent shift between the measurement series is probably due to a somewhat different contact area between needle and electrode.

#### 3.2.2.5 Influence of temperature

Electrodes of the geometry series 2 (area variation) were investigated at varying temperatures. The shape of the impedance spectra remained constant, with only the peak frequency in the Nyquist-plot expectedly decreasing with decreasing temperature. Figure 3.15 shows the Arrhenius-plot for the capacitance. Linearly fitting the data resulted in an activation energy of 0.15 eV.

#### 3.2.2.6 Discussion

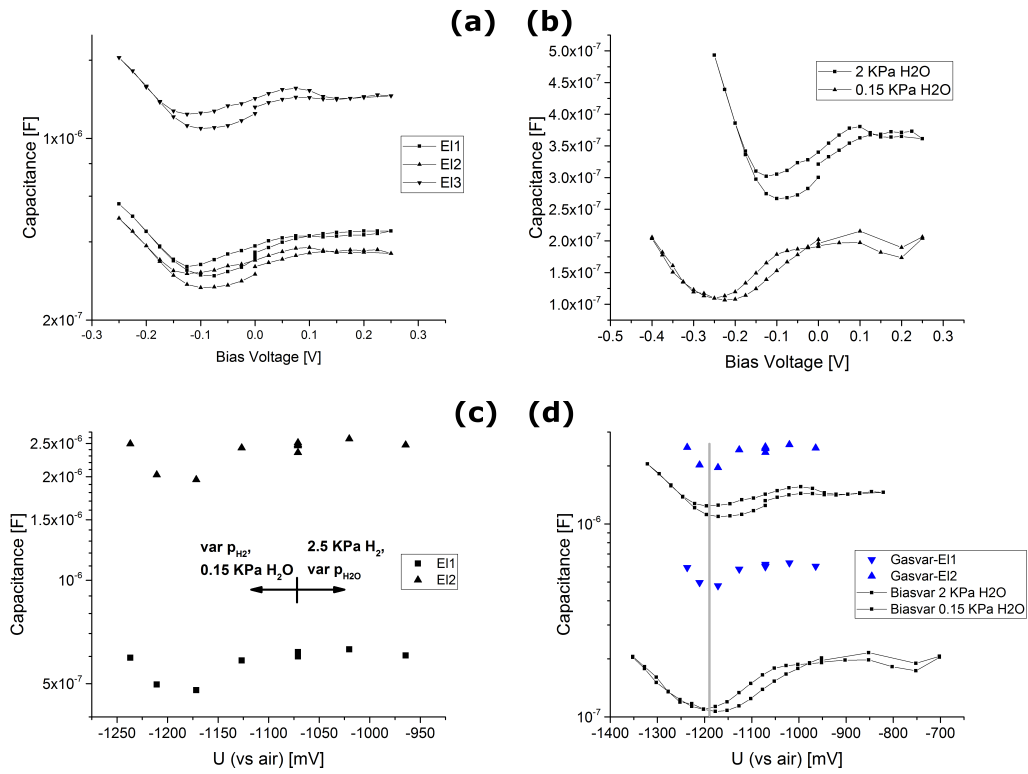


Figure 3.13: Influence of bias voltage and oxygen partial pressure on the capacitance of YSZ/Ni electrodes. (a) Comparison of bias dependency on capacitance for three electrodes. (b) Comparison of bias dependency for electrodes in two different atmospheres. (c) Oxygen partial pressure dependence of the capacitance for 2 electrodes. X-Axis shows Nernst-voltage of the gas vs. air. (d) Combination of bias variation data (from b) and atmosphere variation data (from c) in a Nernst-voltage vs. capacitance plot. The grey line is a guide to the eye. Conditions (unless otherwise noted): 800 °C, 2.5 kPa H<sub>2</sub>/0.15 kPa H<sub>2</sub>O/balance Ar.

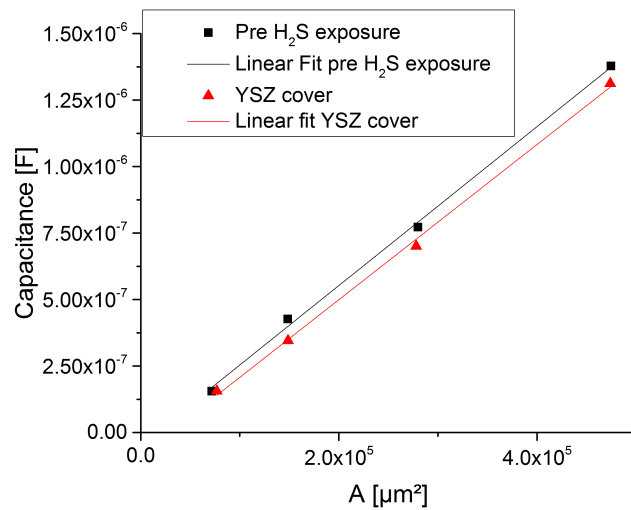


Figure 3.14: Comparison of capacitances of YSZ/Ni electrodes with/without a YSZ8 top layer. Conditions: 800 °C, 2.5 kPa H<sub>2</sub>/0.15 kPa H<sub>2</sub>O/balance Ar.

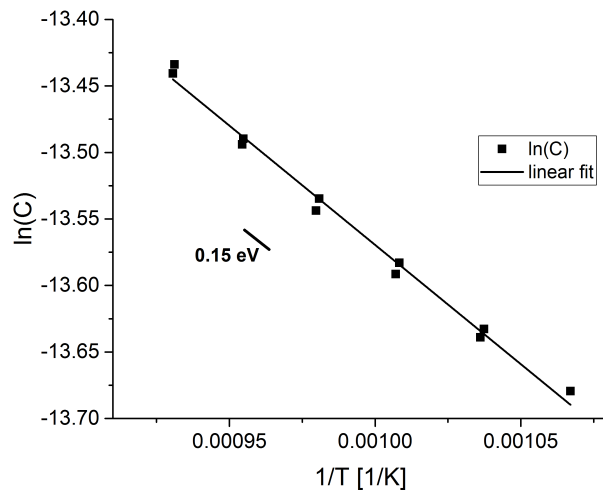


Figure 3.15: Temperature dependence of the capacitance of YSZ/Ni electrodes in an Arrhenius plot. Atmosphere: 2.5 kPa H<sub>2</sub>/0.15 kPa H<sub>2</sub>O/balance Ar.

**Electrostatic models** The most well-known type of electrode/electrolyte interface capacitance is a Helmholtz double layer. In this model electrons and ions form a plate capacitor at the boundary of the electrode and the electrolyte, respectively. The expected ASC of such a plate capacitor in YSZ/Ni electrodes can be estimated by using the formula  $C/A = \frac{\epsilon_0 \times \epsilon_r}{d}$  and assuming the values of the relative permittivity to be  $\epsilon_r = 10$  (bulk YSZ has  $\epsilon_r \sim 27$ , due to high electric fields at the interface lower values are expected), vacuum permittivity to be  $\epsilon_0 = 8.85 \times 10^{-12} \text{ F m}^{-1}$ , and the distance to be  $d = 250 \text{ pm}$  (diameter of an oxide ion). The resulting expected ASC computes as  $0.35 \text{ F m}^{-2}$ , which is an order of magnitude lower than the observed ASC of around  $3 \text{ F m}^{-2}$ . Analogously to previous studies it can therefore be concluded that Helmholtz double layer capacitance cannot fully explain the observed capacitance of YSZ/Ni electrodes. [43, 52]

An alternative electrostatic model based on the Gouy-Chapman diffuse double layer model was proposed by Hendriks et al., which aims at explaining the unusually high ASC in YSZ/Ni electrodes. [55] This model is, however, limited in applicability analogously to the Gouy-Chapman model by the assumption of point-like ions, which can approach the electrode arbitrarily close. An improvement on this model, accounting for the size of ions by combining a Helmholtz and Gouy-Chapman double layer, is the Stern model which has as an upper limit of ASC, which is the ASC of a Helmholtz double layer. [68] It can therefore be concluded that neither a fixed, nor a diffuse double layer can explain the observed ASC values.

Besides the absolute ASC value the rather complex bias voltage/oxygen chemical potential dependency, the hydrogen sulfide influence and the temperature dependence also cannot be explained by the above mentioned models.

**Chemical models** Having shown that electrostatic models cannot explain the capacitive behavior of YSZ/Ni electrodes the question remains as to how these unusually high ASC values can be explained. Since electrostatic capacitances are limited by the density of charge carriers a model explaining the rather high ASC may include a neutralizing/buffering of charge carriers. Such a mechanism can be provided by chemical redox reactions, increasing the potential flow of charge carriers to the interface and thereby the apparent capacitance. Such a type of capacitance with faradaic currents and accumulation of reaction products (like in a battery) is often referred to as chemical capacitances. A chemical capacitance would also be in accordance with other experimental findings, like oxygen chemical potential/bias voltage dependence,  $H_2S$  sensitivity and temperature dependence, as chemical reactions are often coupled to other equilibria in the system (e.g. adsorbate equilibria for multiple species).

The origin of this chemical capacitance can be situated either at the Ni surface, the Ni bulk or the YSZ/Ni interface as the size of all three regions scales linearly with the projected area of the electrodes. Since  $H_2S$  is known in the SOFCs community for adsorbing to the Ni surface and since  $H_2S$  was shown to affect the ASC (cf. figure 3.12), this surface is a natural starting point for investigating the origin of the unusual capacitive behavior of YSZ/Ni electrodes. Assuming the capacitance originates from the surface and chemical changes influence the capacitance a modification of the surface by YSZ deposition on top should have significant influence on the observed ASC. This difference was, however, not found (see section 3.2.2.4). Therefore the capacitive behavior has to originate either from the Ni bulk or the YSZ/Ni interface. As for the sulfur, previous studies found that sulfur can dissolve in Ni (about 40 ppm [69]) where it segregates to grain boundaries. [70] From

these results it is also plausible to assume sulfur to be present at the interface between Ni and YSZ, therefore  $H_2S$  influence on the ASC does not disprove a YSZ/Ni interface origin for the capacitance.

With the above mentioned interpretations in mind the following five capacitive mechanisms are presented. While mechanism (a) will be a mechanism occurring in the Ni bulk (b)-(e) explain the capacitance from interface effects.

(a) Hydrogen reservoir in Ni: In this mechanism hydrogen stored in the Ni bulk diffuses to the TPB and reacts off to form water according to  $2H_{Ni} + O_O^\times \rightarrow H_2O + V_O^\bullet$  (Mechanisms with reaction at the interface are discussed below). For this mechanism to act purely capacitively, both the supply of hydrogen from the surface has to be slow and the reaction at the TPB has to be fast. The former condition appears unrealistic while the latter contradicts the notion of a rate limiting step at the TPB. It can therefore be concluded that this mechanism is not likely to contribute significantly to the overall capacitance of YSZ/Ni electrodes.

(b) Oxygen non-stoichiometry: The most common source of chemical capacitance in mixed ionic-electronic conductors is a change in oxygen stoichiometry resulting in free electron/electron hole formation. A similar mechanism could be occurring in YSZ/Ni electrodes when a reducible oxide is present. In general, chemical capacitance due to stoichiometry changes involving free charge carriers can be estimated by

$$ASC = \frac{e^2 z_i^2}{k_B T} c_i s \quad (3.1)$$

with  $e$  the elementary charge,  $z_i$  the elementary charge per particle  $i$ ,  $k_B$  the Boltzmann constant,  $T$  the temperature,  $s$  the thickness of



the layer and  $c_i$  the concentration of minority charge carriers involved in the process. [71] Assuming oxygen non-stoichiometry in the 1 nm interlayer between Ni and YSZ (see figure 3.6) being responsible for the capacitance an electron concentration (minority charge carrier) of more than  $10^{21} \text{ cm}^{-3}$  is necessary.

Relatedly, the YSZ below the interlayer may be partly reduced. In air non-stoichiometry causes a negligible hole formation, but in strongly reducing conditions, such as cathodically polarized electrodes in  $H_2/H_2O$  atmosphere electron concentration can become significantly high and, for example, at an oxygen partial pressure of  $3.2 \times 10^{-26}$  ( $-1320 \text{ mV vs. air}$  in fig. 3.13d) an electron concentration of  $1.1 \times 10^{20} \text{ cm}^{-3}$  can be estimated. [72] With equation 3.1 a layer thickness of only 15 nm could explain the observed ASC. A detailed analysis of the spatial distribution of oxygen chemical potential in YSZ, which would be necessary to obtain more precise results is, however, beyond the scope of this study.

- (c) Interface impurities: Hansen et al. [43] suggested a capacitive mechanism involving valence changes of impurities segregated to the interface. Since their study used ‘point electrodes’, i.e. Ni wires pressed on YSZ substrates, which have a much higher volume to surface area than thin film pattern electrodes used in this study, a higher ASC is expected in their study. Since ASC values are comparable between Ref. [43] and the present work, impurities do not seem to be the main contributor to the observed ASC. (Assuming no impurities are introduced during sample processing)
- (d) Protons at the interface: As mentioned in Ref [52] the redox couple  $H/H^+$  together with local storage of one of the species could also cause

elevated ASC values. In the context of this system, proton formation at the interface means that water, formed by oxide ions and hydrogen, is stored at the interface as  $OH_{\dot{O}}$ . The reactions in Kröger-Vink notation are  $2H_{Ni} + O_{\dot{O}}^{\times} \rightleftharpoons H_2O + 2e'_{Ni} + V_{\dot{O}}$  and  $H_2O + V_{\dot{O}} + O_{\dot{O}}^{\times} \rightleftharpoons 2OH_{\dot{O}}$ . Electrons from the proton formation are left in the Ni while electrons bound in oxide ions occupy equilibrium-vacancies (the bulk oxide ions are replenished by electrons and oxygen at the counter electrode) which in sum prevents electrostatic charging of the interface. Since YSZ bulk does not incorporate relevant amounts of protons, [73] the protons can only be stored close to the surface, potentially only in the interlayer between Ni and YSZ (see figure 3.6). For this 1 nm thick layer according to equation 3.1 a  $H^+/OH_{\dot{O}}/V_{\dot{O}}$  concentration of  $1.7 \times 10^{21} \text{ cm}^{-3}$  for an ASC of  $3 \text{ F m}^{-2}$  is necessary. This corresponds to about 3 mol% with respect to oxygen lattice sites in YSZ, which is a plausible concentration value.

The measured effect of  $H_2S$  exposure may be explained by sulfur at the YSZ/Ni interface stabilizing oxygen vacancies, thus reducing the capacity for proton absorption. The effect of oxygen chemical potential is qualitatively not clear as several ions may be influenced by it. In conclusion, this mechanism is a plausible mechanism to explain the elevated ASC values in YSZ/Ni electrodes.

- (e) Local Ni oxidation: This mechanism is similar to mechanism b, but with actual phase formation of a nickel (sub)-oxide  $NiO_{1-x}$ . In the most general case of stoichiometry change and Ni metal oxidation the reaction for this mechanism may be formulated as follows:



Since bulk nickel oxide is unstable below an oxygen partial pressure of  $10^{-14}$  bar at 800 °C, [74] it is not expected to be found in the system. Close to the interface, however, a (sub)-oxide may be stable under measurement conditions according to the reaction shown above and might constitute the interlayer between Ni and YSZ in figure 3.6. A similar mechanism for Pt on YSZ has been proposed in air. [63, 75, 76] Regarding the effect of  $H_2S$  on the ASC, suboxide formation at the interface could be influenced by sulfur thus changing the overall ASC. Additionally, at sufficiently low oxygen partial pressures the suboxides are expected to be finally decomposed, reducing the capacitance from this reaction to zero. With an increase of capacitance with decreasing oxygen partial pressure below  $6 \times 10^{-24}$  bar this mechanism is probably only an option for oxygen partial pressures above  $6 \times 10^{-24}$  bar.

### 3.2.3 Electrocatalytic activity

The reader should note that a subset of the data presented in this section have already been published in Ref. [77].

#### 3.2.3.1 Influence of electrode geometry

To revisit the conclusion in previous work, two types of electrode series were investigated: Electrodes with the same area but varying  $l_{TPB}$  and electrodes with the same  $l_{TPB}$  but varying area (new series, see figure 3.1).

Results for the series with varying  $l_{TPB}$  can be seen in figure 3.16, where  $l_{TPB}$  is plotted against the polarization resistance in a double logarithmic diagram. The slope of the fitted line in this diagram corresponds to  $\alpha$  in equation 1.2 and has the value of -0.66. This slope is therefore clearly different from the ideal value of -1 and in loose agreement with values reported of literature (see

section 1.3). In an alternative representation the data are shown in a linear  $1/R_{Pol}$  vs.  $l_{TPB}$  plot in figure 3.17a. Fitting the data linearly results in a line specific conductance of  $2.66 \times 10^{-5} \text{ S m}^{-1}$  and an intercept of  $5.4 \times 10^{-7} \text{ S}$ . It should be noted that the y-intercept is statistically significantly larger than 0 ( $0 \notin CI95\%$ ). A more detailed discussion of residuals in figure 3.17 is given in Ref. [77].

Analogously, results of the electrode series with varying area are shown in a  $1/R_{Pol}$  vs. area plot in figure 3.17b. The plot shows a linear relationship between area and  $1/R_{Pol}$  with an obvious  $1/R_{Pol}$  intercept and a slope larger than 0; the fitted results are an area specific conductance of  $0.21 \text{ S m}^{-2}$  and an intercept of  $1.3 \times 10^{-7} \text{ S}$  (normalized to  $l_{TPB}$   $3.2 \times 10^{-5} \text{ S m}^{-1}$ ). This result means that catalytically active sites are not only located close the TPB, but also at the ‘area’ of the electrode as the activity increases with both the  $l_{TPB}$  and the projected area of the electrode. This observation can be described as 2 parallel reaction pathways (for detailed discussion cf. section 3.2.3.5). The  $1/R_{Pol}$ -intercept for this electrode series will therefore be interpreted as ‘TPB pathway activity’ while the slope will be interpreted as ‘area pathway activity’ in the following chapters.

### 3.2.3.2 Influence of hydrogen sulfide

Electrodes of the geometry series 3 (area variation) were measured before and after exposure to 10 ppm of  $H_2S$ . The resulting area/conductance diagram analogous to section 3.2.3.1 is shown in figure 3.18. It can be seen that while the intercept (TPB activity) decreases from  $1.58 \times 10^{-7} \text{ S}$  to  $8.2 \times 10^{-8} \text{ S}$  by almost 50 % the slope (area pathway activity) decreases from  $0.205 \text{ S m}^{-2}$  to  $0.162 \text{ S m}^{-2}$  by only 20 %.

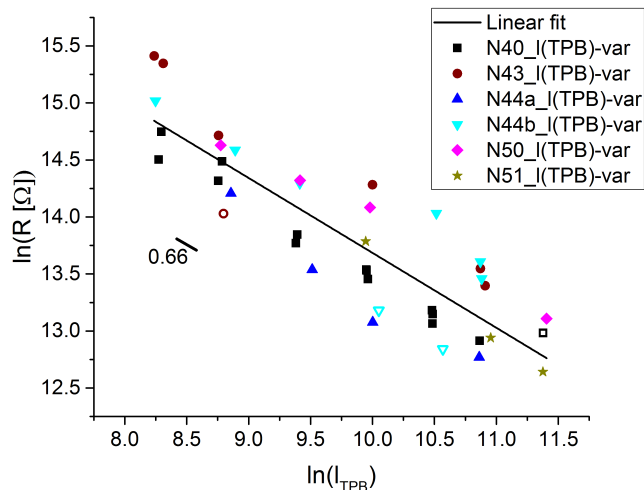


Figure 3.16: Polarization resistance dependence of the TPB length dependency using electrodes with constant area in a double-logarithmic plot. Conditions: 800 °C, 2.5 kPa H<sub>2</sub>/0.15 kPa H<sub>2</sub>O/balance Ar.

### 3.2.3.3 Activation energy

Electrodes of the new series with varying area were electrochemically characterized at different temperatures. The  $1/R_{Pol}$  vs. area diagram with the results is shown in figure 3.19a. It can be seen that the  $1/R_{Pol}$ -intercept as well as the slope significantly increase with increasing temperature. Intercepts and slopes from fits in figure 3.19a as measures of the TPB- and area-pathway activity were fitted in an Arrhenius plot, see figure 3.19b. The fits in the Arrhenius plot revealed an activation energy of 1.96 eV for the TPB pathway, while the area pathway was activated by 1.04 eV.

### 3.2.3.4 Influence of H<sub>2</sub> and H<sub>2</sub>O partial pressures

Reaction orders for hydrogen and water were determined by measuring polarization resistances of electrodes of the new varying area series in different

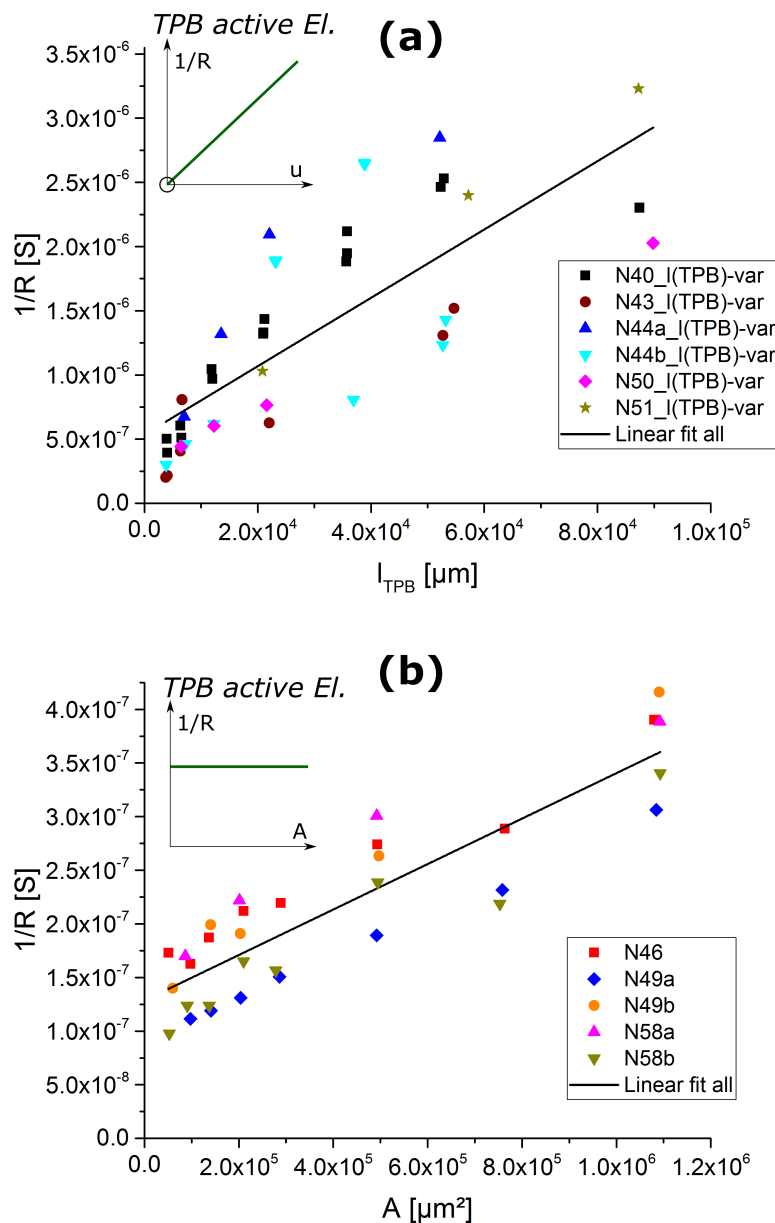


Figure 3.17: Geometry dependency of YSZ/Ni conductance/activity. Inserts show the ideal behavior of solely TPB active electrodes. (a) TPB length dependency for electrodes with constant area. (b) Area dependency of electrodes with constant TPB length (new series). Conditions:  $800^\circ\text{C}$ ,  $2.5\text{ kPa H}_2/0.15\text{ kPa H}_2\text{O}/\text{balance Ar}$ .

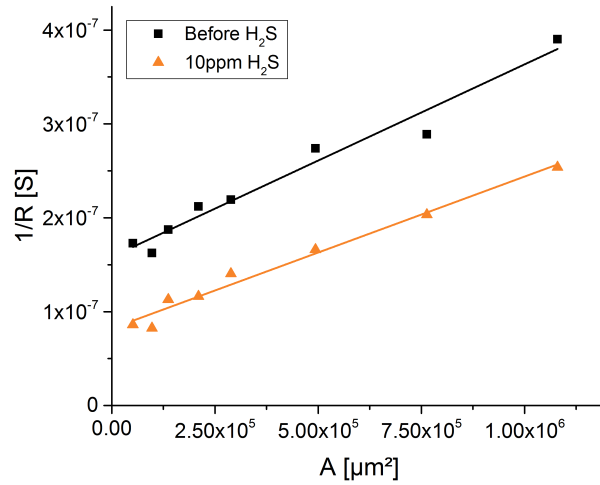


Figure 3.18: Area dependent effect of 10 ppm  $H_2S$  exposure on electrodes of the geometry series 3 (area variation). Conditions: 800 °C, 2.5 kPa  $H_2$ /0.15 kPa  $H_2O$ /balance Ar.

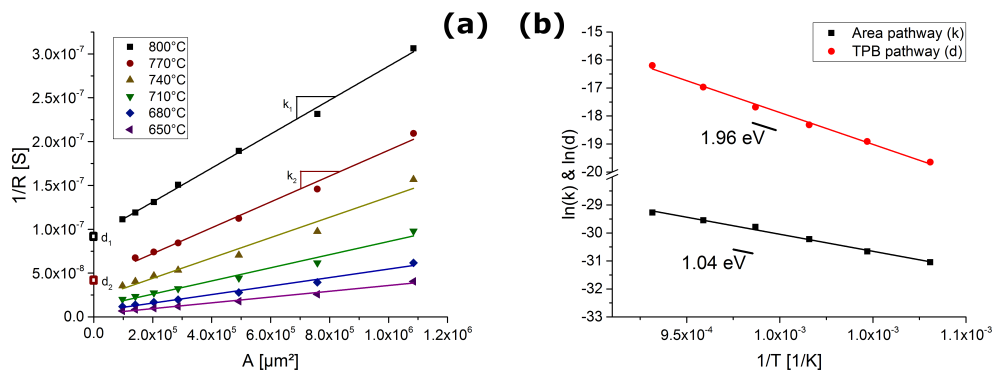


Figure 3.19: Temperature dependence of  $1/R_{Pol}$  of YSZ/Ni electrodes. (a) Area vs. conductance at different temperatures with linear fits. (b) Slopes  $k$  and  $1/R_{Pol}$ -intercepts  $d$  in an Arrhenius diagram. Atmosphere: 2.5 kPa  $H_2$ /0.15 kPa  $H_2O$ /balance Ar.

atmospheres. Assuming the atmospheric partial pressures to be present at the reaction sites (fast diffusion) and a simple power law for the reaction rate the partial reaction order  $\zeta_x$  for a reactant  $x$  can be easily determined in a double-logarithmic diagram using the equation

$$\log(1/R_{Pol}) = \zeta_x \times \log(p_x) + \log(1/R_{Pol,0}) \quad (3.2)$$

with  $p_x$  the partial pressure of the reactant and  $R_{Pol,0}$  a constant. It should be noted that this relationship still holds true when the inverse polarization resistance is exchanged with geometrically normalized  $1/R_{Pol}$ .

To obtain pathway-specific reaction orders,  $1/R_{Pol}$  data were plotted as a function of the electrode area for all measured gas compositions; some gas composition data are shown in figure 3.20. Since for all gas compositions a linear relationship was found, the fitted slopes and  $1/R_{Pol}$ -intercepts were plotted in double-logarithmic diagrams against the corresponding hydrogen and water partial pressures, see figure 3.21. From linear fits in these double-logarithmic diagrams the reaction orders were computed according to equation 3.2. For hydrogen this resulted in a reaction order of 0.38 for the TPB pathway (figure 3.21d) and 0.50 for the area pathway (figure 3.21a). For water the reaction order for the TPB pathway was 0.35 and also 0.35 for the area pathway. Additionally, the oxygen equilibrium partial pressure for the gas mixtures was calculated using NIST data [67], which were plotted against  $1/R_{Pol}$  analogously to hydrogen and water, see figure 3.21c&f. In these diagrams no linear trend could be found, hence no reaction order for oxygen could be obtained.

### 3.2.3.5 Discussion



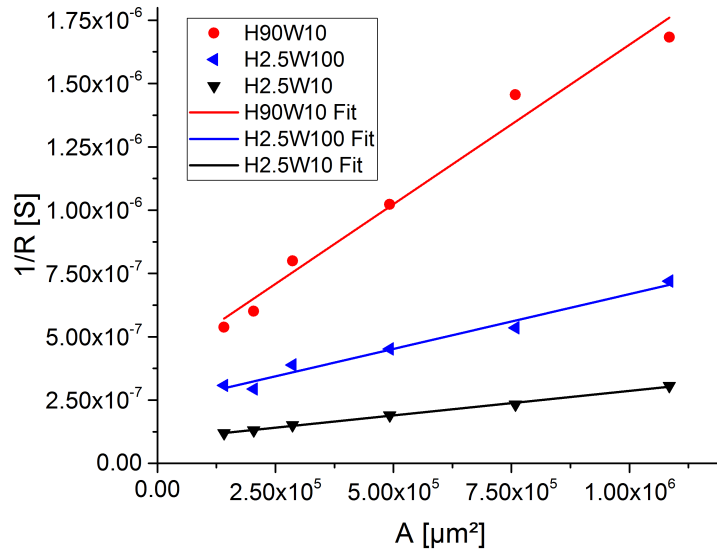


Figure 3.20:  $1/R_{Pol}$  vs. area diagrams for YSZ/Ni electrodes in different atmospheres. Conditions: 800 °C, H90W10 = 90 kPa H<sub>2</sub>/0.15 kPa H<sub>2</sub>O/balance Ar, H2.5W100 = 2.5 kPa H<sub>2</sub>/1.5 kPa H<sub>2</sub>O/balance Ar, H2.5W10 = 2.5 kPa H<sub>2</sub>/0.15 kPa H<sub>2</sub>O/balance Ar.

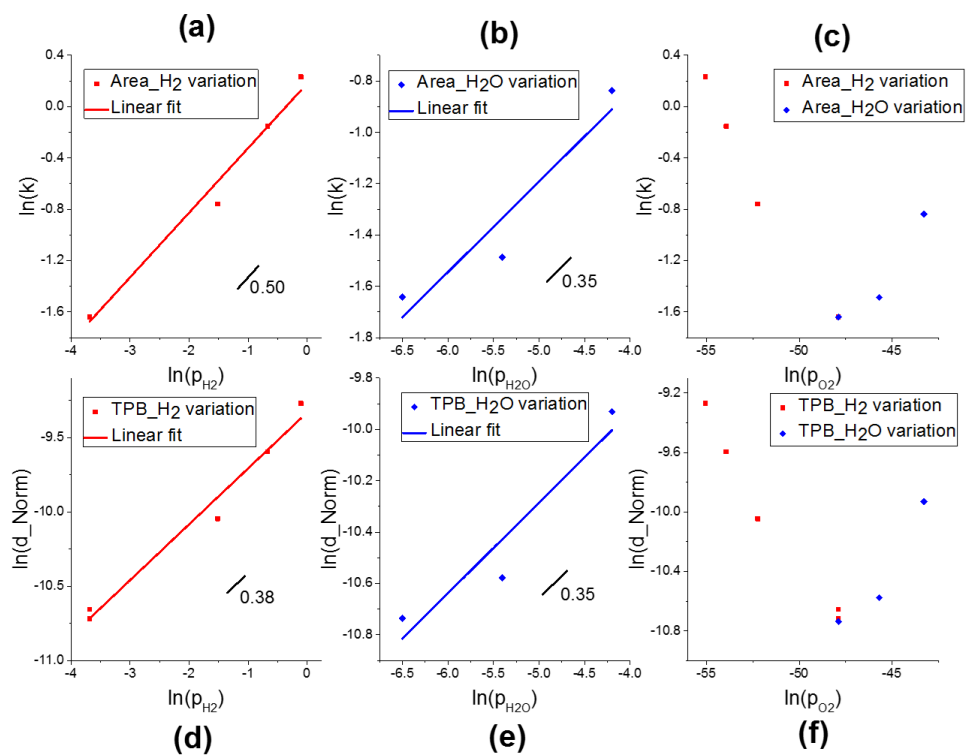


Figure 3.21: Reaction order determination for hydrogen and water on YSZ/Ni electrodes. (all pressures in bar) (a-c) Area pathway data, (d-f) TPB pathway data. (a,d)  $p_{H_2}$  variation with water partial pressure of 0.15 kPa, (b,e)  $p_{H_2O}$  variation with hydrogen partial pressure of 2.5 kPa. (c,f) Conductance of data to the left as a function of equilibrium oxygen partial pressure. Temperature: 800 °C.

**Reaction pathways** On heterogeneous catalysts the reaction rate is determined by active sites where the rate limiting step takes place. Assuming equal reaction rates at each active site (or an average rate for an ensemble of sites) the reaction rate is expected to be proportional to the number of available active sites. If those active sites are also located in specific spatial parts of the catalyst, the location of active sites can be pinpointed by testing for proportionality of macroscopic reaction rates and size of the suspected active location. In case of Ni on YSZ and a suspected TPB-activity this means that proportionality between  $l_{TPB}$  and reaction rate - which in turn is proportional to  $1/R_{Pol}$  - is expected. Using equation 1.2 this proportionality would be equivalent to a line with a slope of -1 in a double logarithmic  $l_{TPB}$  vs.  $R_{Pol}$  diagram. Literature data suggest some deviation from a slope of -1 (cf. section 1.3) and this study also found deviation from this value (cf. section 3.2.3.1) using a substantially larger statistical sample size than in literature. Hence, the mechanistic picture of an ideal TPB active electrode is doubtful.

Deviations from the ideal slope of -1 in figure 3.16 have been explained in different ways: Bieberle et al. [53] assumed underestimation of  $l_{TPB}$  in geometric measurements due to defects in the Ni layer. Yao and Croiset [48] alternatively assumed other limiting processes in series like water diffusion in the setup to cause the deviation. In this study no defects causing more  $l_{TPB}$  in the Ni layer could be found even in high magnification SEM images (cf. figure 3.2) and, since needle contacting doesn't constrict gas transport, gas diffusion polarization can be neglected. Hence, the aforementioned non-proportional scaling must have a different explanation.

One possible explanation for the unexpected scaling of  $R_{Pol}$  is an additional activity, which does not scale with  $l_{TPB}$ . This hypothesis entails that in a

$1/R_{Pol}$  vs.  $l_{TPB}$  diagram a linear relationship between the properties can be found as this additional parallel path offsets the TPB related conductance/activity. This linear relationship can indeed be seen in figure 3.17a. The origin of the additional activity offsetting the TPB activity must be in additional active sites not located at or close to the TPB.

A promising candidate for the location of the additional active sites is the ‘area’ of the electrode since the projected area of all electrodes in the series measured in figure 3.17a are nominally the same. The hypothesis of an additional area related pathway (i.e. with a rate limiting step at/in the electrode’s surface/bulk/interface) demands a linear relationship between the electrode area and  $1/R_{Pol}$  for electrodes with the same TPB length. Additionally, in case no further pathway is present, the offset of the area related activity should be consistent with the TPB activity. Figure 3.17b shows the aforementioned linear relationship between area and  $1/R_{Pol}$ . Also, the offset normed to the  $l_{TPB}$  (see section 3.2.3.1) is  $3.2 \times 10^{-5} \text{ S m}^{-1}$ , which is in reasonable agreement with the TPB specific conductance of  $2.66 \times 10^{-5} \text{ S m}^{-1}$  in the  $l_{TPB}$  variation series. It can therefore be concluded that there are two significant reaction pathways in the YSZNi system - a ‘TPB pathway’ and an ‘area pathway’.

**Reaction pathway properties** Having shown the existence of two individual reaction pathways, properties of both may be compared. To obtain more precise results, electrodes of the geometry series 3 (area variation) were measured under different conditions as this series allows for a better separation of TPB- and area-effects (cf. section 3.2.1.1).

The effect of  $H_2S$  exposure on the conductance for electrodes with different geometries, as shown in section 3.2.3.2, highlights that the newly found

area pathway has different electrochemical properties compared to the TPB pathway as it is more resilient to sulfur poisoning.

The activation energy of the rate limiting steps of both pathways can be determined by measuring electrodes of the geometry series 3 (area variation) at different temperatures. As figure 3.19 shows, the activation energies for the pathways is significantly different, with the rate limiting step of the area pathway having a smaller activation energy of 1.04 eV and the TPB pathway being activated by 1.96 eV. This significant difference in properties further shows that both pathways are of different nature and could not originate from unaccounted  $l_{TPB}$ . Comparing the values reported in this thesis to literature values is not straightforwardly possible, as previous work did not account for two reaction pathways. Under certain circumstances, however, 2 different activation energies could have been observed: A higher activation energy at high temperatures and a lower at low temperatures as both pathways are in parallel. This qualitative result was indeed found by Yao and Croiset, although with different absolute values for the activation energy. [48] Absolute activation energy values scatter greatly in literature (cf. section 1.3) without a commonly accepted explanation, hence no direct conclusions can be drawn from the absolute value of this property.

Partial reaction orders of the reactants include information about a subset of reaction steps in the reaction chain. This is due to non-rate limiting steps being in a quasi-equilibrium, whose equilibrium reactant concentrations can be influenced by hydrogen and water partial pressures. The reactant concentrations in the rate limiting step, which in turn determine the reaction rate, can therefore vary because of the ‘feedback’ from the aforementioned influenced reaction steps. Hence, reaction orders may be seen as an unspecific probe also for non-rate limiting steps. While inference from such an unspecific probe is

not straightforward, under certain circumstances conclusions may be drawn from the obtained reaction orders: In the YSZ/Ni system the reaction chain for hydrogen oxidation (water reduction) must start and end with gaseous  $H_2$  and  $H_2O$  and oxide ions in YSZ for both pathways. Somewhere in the reaction chain the pathways must split up to then reunite after the rate limiting step at some point. If a species only influences reaction steps where both pathways are united, then the reaction order for this species should be the same for both pathways. This equality of reaction orders was found in the case of water, which, combined with the non-trivial reaction order, is an indication that some reaction steps are shared between the pathways.

**Reaction mechanism** Based on the above shown results and interpretation thereof two possible hydrogen oxidation reaction mechanisms for the newly discovered area pathway were constructed: In the first ‘proton diffusion mechanism’, illustrated in figure 3.22b, hydrogen moves towards the YSZ. After adsorption on the Ni surface and diffusion through the nickel a charge transfer reaction occurs at the interface. The resulting protons then diffuse along the interface to the TPB where they react off forming water. Pathway convergence occurs at the TPB, where protons formed there and area pathway-originating protons both react with oxide ions to  $H_2O$  which desorbs. In the area pathway of this reaction mechanism only hydrogen adsorption, hydrogen diffusion through Ni, and the charge transfer reaction may be rate limiting, as the other processes would not yield a linear scaling with the projected electrode area. This also means that proton diffusion along the YSZ/Ni interface must be fast. Since no composition of the 1 nm thick interlayer found between Ni and YSZ could be determined, estimations as to the diffusion coefficient are not possible. At these elevated temperatures fast proton diffusion, even at macroscopic scales of the electrodes (maximally

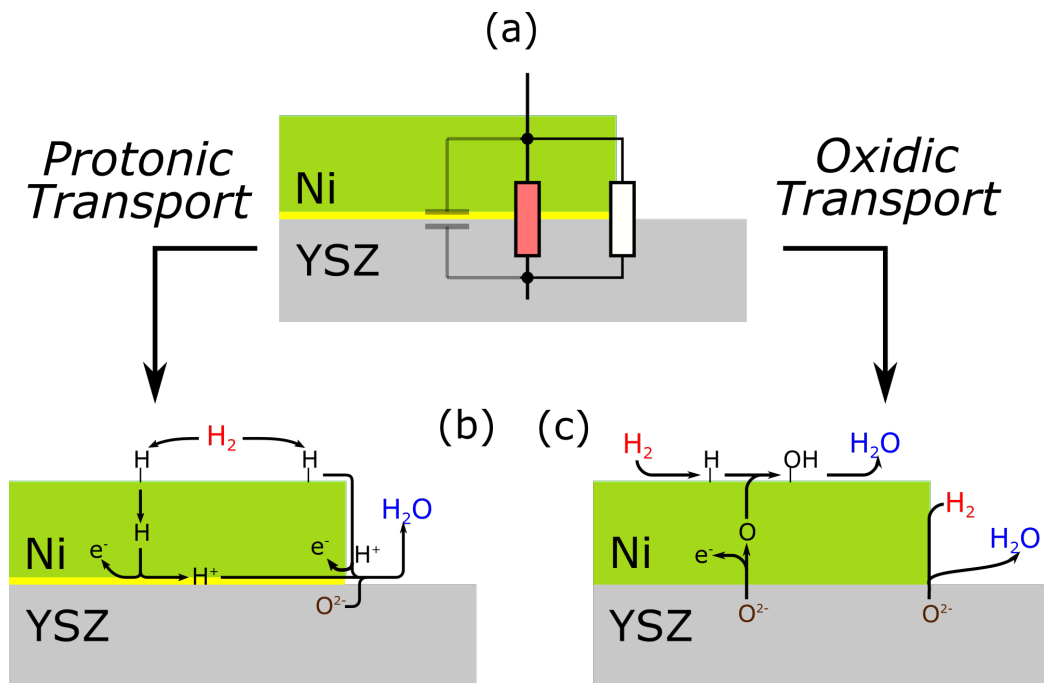


Figure 3.22: Possible reaction mechanism for hydrogen oxidation in YSZ/Ni electrodes. (a) Equivalent circuit to be explained with area- and TPB-pathway. (b) Protonic transport mechanism. (c) Oxidic transport mechanism.

600  $\mu\text{m}$ ) is feasible. From the above mentioned principally possible rate limiting steps dissociative hydrogen adsorption at the surface may be regarded as fast. [78] In case hydrogen bulk diffusion through Ni is limiting the expected polarization resistance  $R_{diff}$  can be calculated using

$$R_{diff} = \frac{k_B T}{z^2 e^2} \frac{L_D}{D n_{eq}} \quad (3.3)$$

with  $k_B$  the Boltzmann constant,  $T$  the temperature,  $z$  the number of elementary charges per reaction unit,  $e$  the elementary charge,  $L_D$  the diffusion length,  $D$  the diffusion coefficient and  $n_{eq}$  the equilibrium concentration of the species. Using the values of  $T = 800^\circ\text{C}$ ,  $z = 1$ ,  $L_D = 1.2 \mu\text{m}$  (electrode thickness),  $D = 9.4 \times 10^{-5} \text{ cm}^2 \text{ s}^{-1}$  [79] and  $n_{eq} = 4.2 \times 10^{-4} \text{ n/n}\%$  [79] a conductance of  $1/R_{Pol} = 2.8 \times 10^3 \text{ S m}^{-2}$  follows. This conductance is 4 orders of magnitude higher than the observed value of  $0.21 \text{ S m}^{-2}$ , hence bulk diffusion of hydrogen through Ni cannot be the rate limiting step of the reaction. Therefore, only rate limiting charge transfer at the YSZ/Ni interface remains as a candidate.

A second possible reaction mechanism for hydrogen oxidation, the ‘oxide diffusion mechanism’, is the ‘reverse’ case where oxygen moves from the YSZ bulk towards the Ni surface as illustrated in figure 3.22c. While the reaction pathways appear disconnected in the figure a convergence occurs on the Ni surface assuming water desorption from the Ni surface in the TPB pathway (‘oxygen spillover’ mechanism in literature [61]). Analogous to the proton diffusion mechanism water desorption from the Ni surface, oxygen diffusion through the Ni bulk or charge transfer by oxide ions may be rate limiting. Estimating bulk diffusion conductance using equation 3.3 with the values  $T = 800^\circ\text{C}$ ,  $z = 2$ ,  $L_D = 1.2 \mu\text{m}$  (electrode thickness),  $D = 5.1 \times 10^{-10} \text{ cm}^2 \text{ s}^{-1}$  [80], and  $n_{eq} = 1.7 \times 10^{-2} \text{ n/n}\%$  [80] a conductance of  $1/R_{Pol} = 2.6 \text{ S m}^{-2}$



is computed. This conductance, while still being one order of magnitude too high, could explain the observed conductance, as data in Ref. [80] are measured in oxygen saturated Ni. Since measurement conditions are more reducing the oxygen concentration is overestimated, which would also lead to an overestimation of the conductance.

**Role of electronic conductivity of YSZ** YSZ is known as a good oxide conducting electrolyte, which entails a good ionic conductivity while being electronically blocking. In practice, however, some electronic conductivity is still present. This electronic conductivity may provide an ohmic path from the working electrode to the counter electrode feigning a genuine electrochemical area pathway. To estimate the conductance of such an ohmic pathway some information about current paths in the electrolyte is needed. This information can be obtained from the ionic spreading resistance, since ions can be expected to spread the same way as electrons in a homogeneous electrolyte. The ohmic resistance of the electronic pathway may therefore be calculated by

$$\frac{\sigma_{eon}}{\sigma_{ion}} = \frac{R_{ion}}{R_{eon}} \quad (3.4)$$

with  $\sigma_x$  the ionic and electronic conductances of YSZ and  $R_x$  the ionic and electronic spreading resistances. Under the standard conditions of 800 °C, 2.5 kPa  $H_2$  and 0.15 kPa  $H_2O$  (equilibrium  $p_{O_2}$  of  $1.6 \times 10^{-19}$  kPa)  $\sigma_{eon} = 1.24 \times 10^{-6}$  S cm<sup>-1</sup> [72] and  $\sigma_{ion} = 3.92 \times 10^{-2}$  S cm<sup>-1</sup> [63] follow. With the ionic spreading resistance of the largest electrode in the geometry series 3 (area variation)  $R_{ion} = 125 \Omega$  an electronic resistance of 3.9 M $\Omega$  follows. The purely area-pathway share of the polarization resistance of the electrode is 4.4 M $\Omega$ , which is in notable agreement with the predicted value for the

electronic pathway. However, several objections against this ohmic pathway feigning an electrochemical pathway may be raised:

- Geometry dependence: For circular electrodes on a infinitely extended electrolyte the spreading resistance is inversely proportional to the electrode diameter. [81, 82] Since the electrodes in the geometry series 3 (area variation) are close to circles the relation  $\frac{1}{R_{Pol,area}} \propto \sqrt{A}$  for the area pathway conductance should hold. Since figure 3.17b shows no such dependency electronic conductance in the electrolyte is an unlikely source of the observed conductance
- Partial pressure dependency: Electronic conductivity in YSZ is proportional to  $p_{O_2}^{-1/4}$ . [72] While for hydrogen the reaction order fits (an  $H_2$  reaction order of 0.51 is equivalent to an  $O_2$  reaction order of 0.26) this prediction, the catalytic effect of water contrasts with the partial pressure dependency prediction.
- Activation energy: The observed activation energy of 1.04 eV does not fit the predicted 3.88 eV for the electronic conductance in YSZ. [72] At e.g. 650 °C the measured area pathway polarization is 24 M $\Omega$ , while the calculated electronic conductance is 650 M $\Omega$  (also corrected for  $p_{O_2}$  temperature dependency).

With the above mentioned objections showing that no significant electronic conductance could be observed in the experimental data the question remains as to why the electronic conductance cannot be seen. One possible explanation is that the interlayer between Ni and YSZ, shown in figure 3.6, acts as an insulator between Ni and YSZ. Alternatively, a Schottky barrier may create a highly resistive interface between Ni and YSZ blocking electrons

from crossing the barrier. Further investigations into this topic are, however, beyond the scope of this thesis.

## 3.3 Variation of the metal and ceramic phase

In this section either Ni is replaced by another metal or the ceramic phase underneath the Ni is replaced by another ceramic to create different types of TPB. If not otherwise noted, impedance spectra were qualitatively equivalent to YSZ/Ni electrodes and were fitted the same way.

### 3.3.1 Platinum on yttria stabilized zirconia

#### 3.3.1.1 Reaction pathways

Analogously to section 3.2.3.1 the geometry dependence of Pt/YSZ electrodes was measured with electrodes of the geometry series 3 (area variation). The resulting area dependence of the  $1/R_{Pol}$  is shown in figure 3.23. As the figure shows, again two reaction pathways seem to be present (fit data summarized in table 3.2). The area pathway activity, indicated by the slope, is very similar to that of YSZ/Ni electrodes under standard measurement conditions, while the TPB pathway seems to be more active by a factor of two under standard measurement conditions.

#### 3.3.1.2 Activation energy

Measurement of Pt/YSZ electrodes of the geometry series 3 (area variation) at different temperatures, analogously to section 3.2.3.3, results in an Arrhenius diagram for the area and TPB pathway as shown in figure 3.24. The fit results are also summarized in table 3.2. It can be seen that while the TPB pathway shows a similar activation energy (2.2 eV) to that of YSZ/Ni electrodes the area pathway is higher activated (1.5 eV). The similar area pathway activities at 800 °C mentioned above are therefore coincidental.

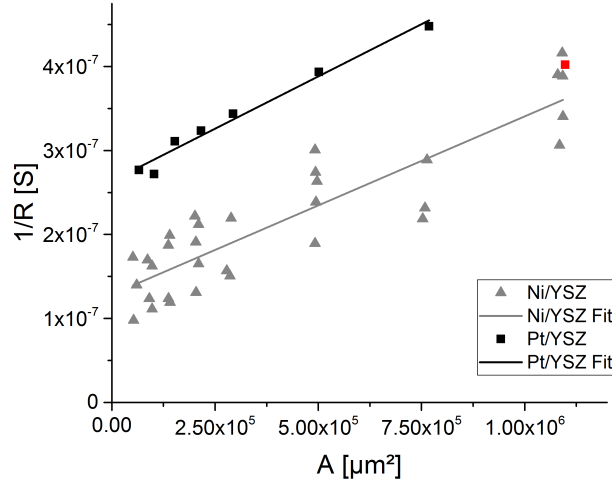


Figure 3.23: Conductance as a function of area for Pt/YSZ electrodes of the geometry series 3 (area variation). YSZ/Ni electrodes are shown for comparison. Conditions: 800 °C, 2.5 kPa H<sub>2</sub>/0.15 kPa H<sub>2</sub>O/balance Ar.

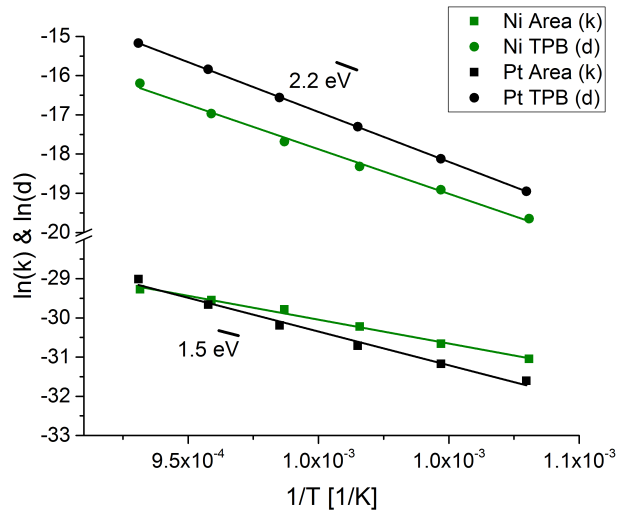


Figure 3.24: Activation energy determination for Pt/YSZ electrodes analogously to section 3.2.3.3. Atmosphere: 2.5 kPa H<sub>2</sub>/0.15 kPa H<sub>2</sub>O/balance Ar.

### 3.3.1.3 Influence of $H_2$ and $H_2O$ partial pressures

Analogously to section 3.2.3.4, water and hydrogen partial pressure dependency of Pt/YSZ electrodes of the geometry series 3 (area variation) was measured. Figure 3.25 shows the resulting reaction order diagrams and table 3.2 summarizes the results. From these results it can be seen that both electrode types show very similar reaction orders for hydrogen, but qualitatively different dependency on water partial pressure with Pt/YSZ electrodes being inhibited by higher water partial pressures. Additionally, a reaction order for oxygen partial pressure could be fitted for Pt/YSZ, which was not possible for YSZ/Ni.

### 3.3.1.4 Discussion

Regarding the catalytic activity and activation energy of Pt/YSZ, interesting comparisons to YSZ/Ni can be made. For the TPB pathways very similar activation energies were measured (see table 3.2), but different activities. This could indicate that the same reaction step is rate limiting for both electrode types while only the number of available reaction sites per  $l_{TPB}$  differs. For the area pathway, however, it seems that a different reaction step (or the same in a different chemical environment) is rate limiting.

The most striking difference between YSZ/Ni and YSZ/Pt electrodes can be seen in the hydrogen/water/oxygen reaction orders. Here, for Pt electrodes water is not catalyzing the hydrogen oxidation as it does for Ni electrodes. Instead, it is possible that the equilibrium oxygen partial pressure is the determining factor in the catalytic activity. These results suggest a different reaction mechanism for both the TPB as well as the area pathway on Pt/YSZ electrodes as compared to YSZ/Ni electrodes. Since reaction orders also

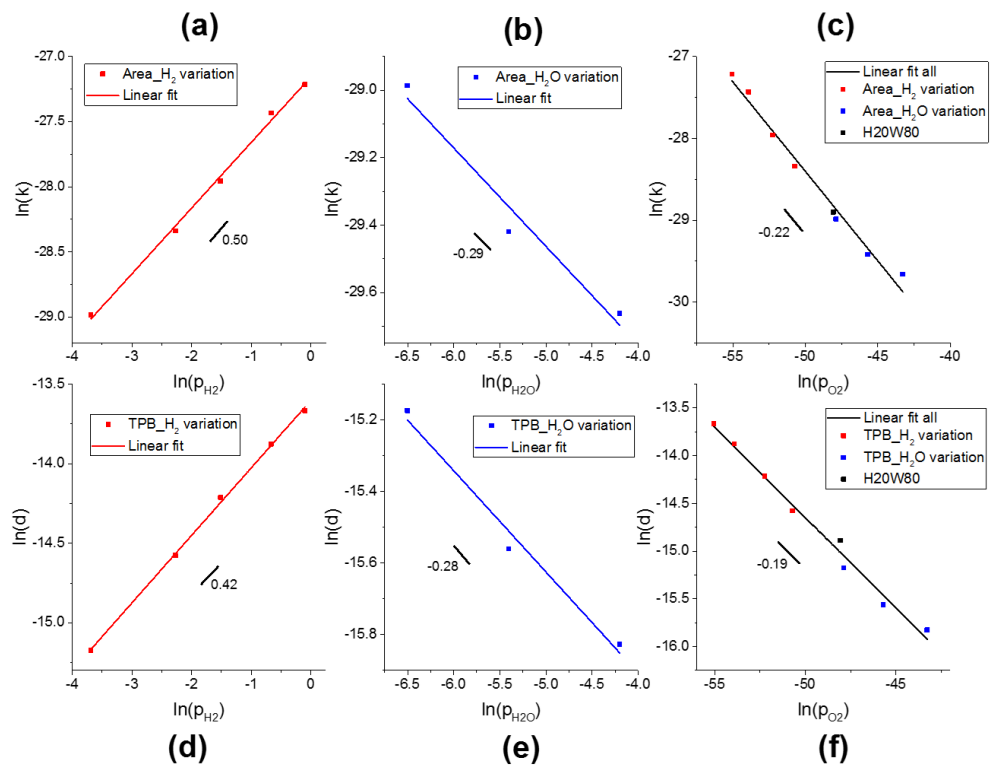


Figure 3.25: Reaction order determination for hydrogen, water, and oxygen on Pt/YSZ electrodes analogously to section 3.2.3.4 ( $1/R_{Pol}$  intercepts not normalized, pressures in bar). Temperature: 800 °C.

probe non-rate limiting steps, the rate limiting step for the YSZ/Ni and Pt/YSZ TPB pathway may still be the same.

### **3.3.2 Nickel on scandia stabilized zirconia**

#### **3.3.2.1 Reaction pathways**

Analogously to YSZ/Ni (section 3.2.3.1) electrodes of the geometry series 3 (area variation) were measured under standard conditions. The resulting conductances are shown in figure 3.26. It can be seen that conductance values are similar to values found in YSZ/Ni electrodes. Linear fitting reveals an area specific conductance of  $0.137 \text{ S m}^{-2}$  and a length specific conductance of  $3.77 \times 10^{-5} \text{ S m}^{-1}$ . Assuming random sampling, a normal distribution (which is doubtful), and equal variance of the data series the area specific conductances of YSZ/Ni and Ni/SSZ are statistically significantly different. ( $p = 0.045$ )

#### **3.3.2.2 Activation energy**

An Arrhenius diagram for the area and TPB pathway was measured on electrodes of the geometry series 3 (area variation) analogously to section 3.2.3.3. The diagram for Ni/SSZ is shown in figure 3.27. It can be seen that the activation energy for the area pathway is 1.13 eV, while the activation energy for the TPB pathway is 1.63 eV.

#### **3.3.2.3 Influence of $H_2$ and $H_2O$ partial pressures**

Hydrogen and water reaction orders were measured analogously to section 3.2.3.4. The reaction order diagrams are shown in figure 3.28. It can be seen that no significant differences in the hydrogen reaction orders compared to YSZ/Ni can be found. Water reaction orders are, however, somewhat



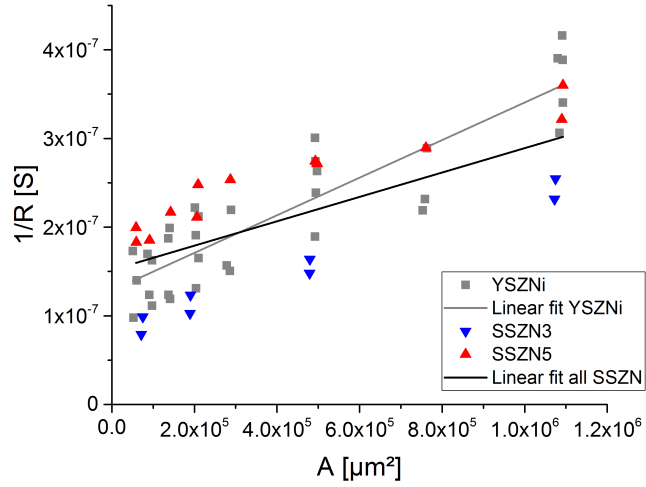


Figure 3.26: Conductance as a function of area for Ni/SSZ electrodes of the geometry series 3 (area variation). YSZ/Ni electrodes are shown for comparison. Conditions: 800 °C, 2.5 kPa H<sub>2</sub>/0.15 kPa H<sub>2</sub>O/balance Ar.

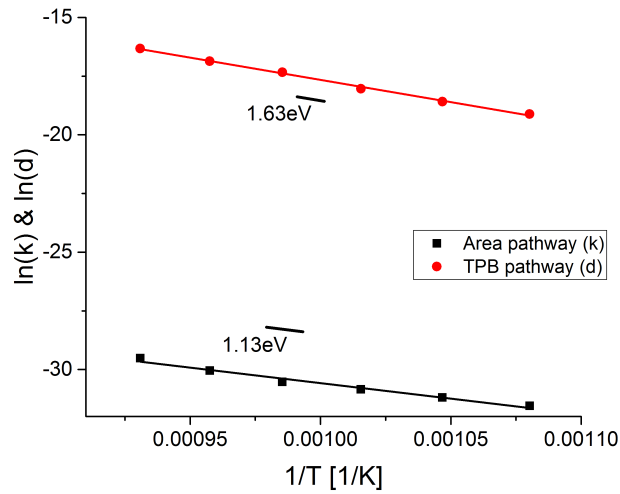


Figure 3.27: Activation energy determination for Ni/SSZ electrodes analogously to section 3.2.3.3. Atmosphere: 2.5 kPa H<sub>2</sub>/0.15 kPa H<sub>2</sub>O/balance Ar.

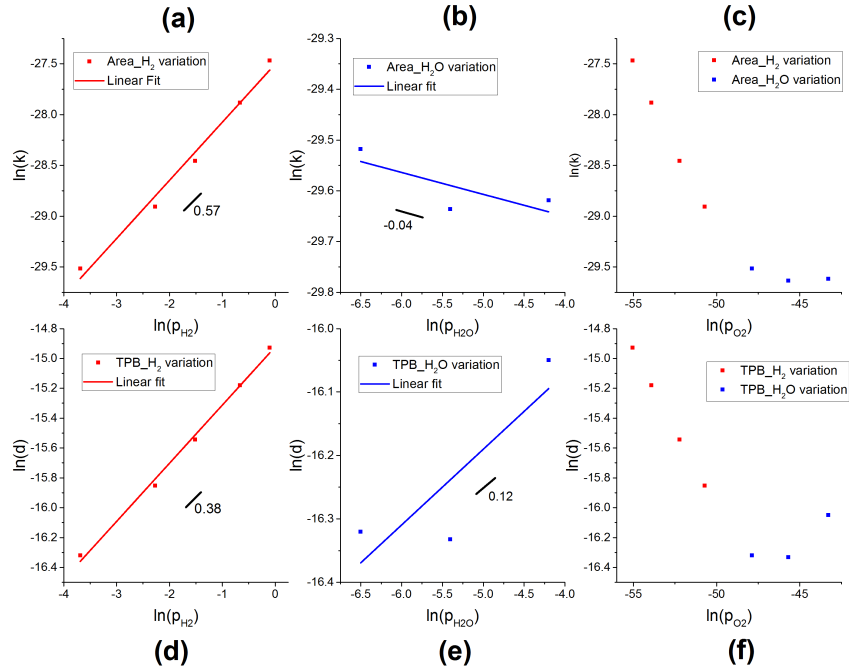


Figure 3.28: Reaction order determination for hydrogen, water, and oxygen on Ni/SSZ electrodes analogously to section 3.2.3.4 ( $1/R_{Pol}$  intercepts not normalized, pressures in bar). Temperature: 800 °C.

different to YSZ/Ni electrodes. Like YSZ/Ni no oxygen reaction order could be determined.

### 3.3.2.4 Discussion

The results of this section shows that while the metal phase does not seem to influence the rate limiting step of the TPB pathway (section 3.3.1) the type of zirconia apparently has some influence as the activation energy difference shows. The area pathway may also be less active, but does have a very similar activation energy to YSZ/Ni, indicating the same rate limiting step. Regarding the hydrogen reaction order, similar values can be found

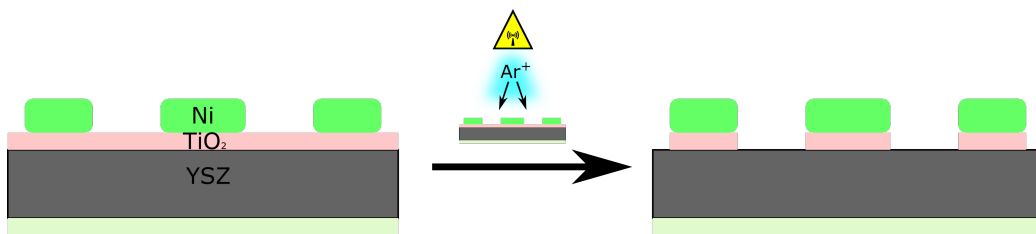


Figure 3.29: Sketch of titania samples used in this thesis. Left: Native titania layer sample covering all the YSZ surface. Middle: Argon ion etching process. Right: Resulting etched titania layer sample. Titania not covered by Ni is removed.

for YSZ/Ni, YSZ/Pt and SSZ/Ni for both the area and TPB pathway, respectively. This similarity is interesting as neither the metal phase nor the zirconia phase seems to have a strong influence on the reaction order.

### 3.3.3 Nickel on titania

To investigate the electrochemical properties of Ni/ $TiO_2$  electrodes (an electrode type currently unknown as SOFC anode) a 30 nm thick sputtered Ti layer, which was deposited on (111)YSZ single crystals and subsequently equilibrated for 3 h in air, was used as a substrate for the usual Ni deposition and structuring. According to Ref. [83] this procedure should mainly result in an anatase layer. To gain more understanding of this type of electrode, not only the native full-titania-layered sample was investigated, but also a sample where in the last step the non-Ni-covered titania layer was removed by Ar beam ion etching; the process is sketched in figure 3.29.

#### 3.3.3.1 Impedance spectrum

For electrodes with a non-etched titania layer the Nyquist plot for a typical impedance spectrum is shown in figure 3.30a. The Nyquist plot shows two main features, which appear like depressed semicircles with a small shoulder

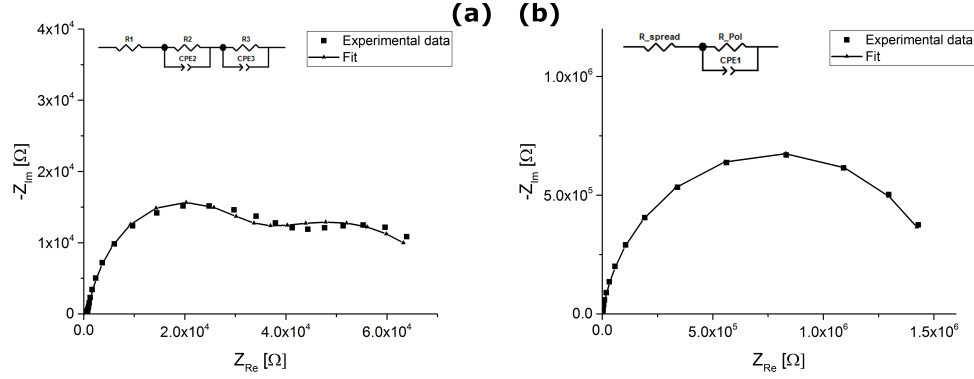


Figure 3.30: Impedance spectra (Nyquist plots) of Ni/ $TiO_2$ /YSZ electrodes. (a) Native  $TiO_2$  layer with fitting line and equivalent circuit as insert. (b) Ion etched  $TiO_2$  layer with fitting line and equivalent circuit as insert. Conditions: 800 °C, 2.5 kPa  $H_2$ /0.15 kPa  $H_2O$ /balance Ar.

in the high frequency range. In order to extract a meaningful polarization resistance the spectrum was fitted using the equivalent circuit shown in figure 3.30a in the frequency range of 100 Hz to 5 mHz and adding up  $R_1$ ,  $R_2$ , and  $R_3$  to yield the total polarization resistance.

In the case of etched titania layers, spectra like the one shown in figure 3.30b are obtained. In this spectrum only one main feature can be found - a depressed semicircle (a tiny shoulder in the high frequency range can safely be ignored in this discussion of rate determining processes). This spectrum was fitted with the equivalent circuit depicted in figure 3.30b in the frequency range of 100 Hz to 5 mHz, and exclusively  $R_{Pol}$  was used for subsequent discussion of electrode polarization resistances.

### 3.3.3.2 Reaction pathways

Electrodes of the geometry series 3 (area variation) were characterized on both native and ion-etched titania layers, the resulting  $1/R_{Pol}$  vs. area diagrams are shown in figure 3.31 and results summarized in table 3.2. The

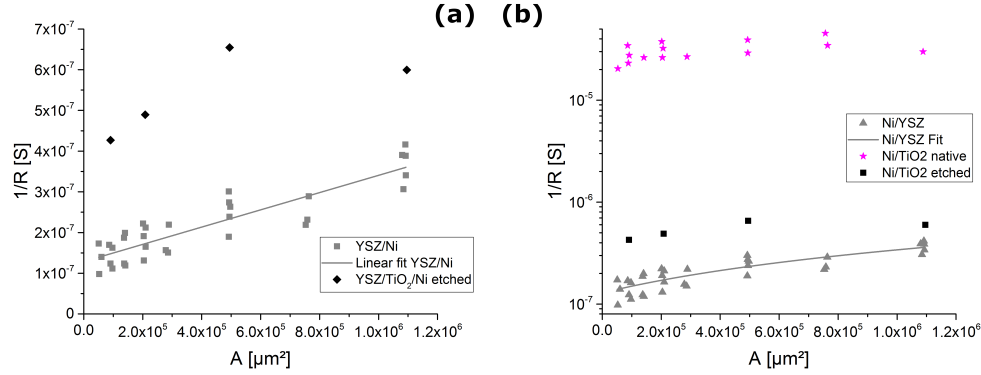


Figure 3.31: Conductance as a function of area for  $YSZ/TiO_2/Ni$  electrodes of the geometry series 3 (area variation). (a) Linear conductance axis with ion etched samples. (b) Logarithmic axis with ion etched and native layered samples.  $YSZ/Ni$  electrodes are shown for comparison. Conditions: 800 °C, 2.5 kPa  $H_2$ /0.15 kPa  $H_2O$ /balance Ar.

comparison with  $YSZ/Ni$  electrodes shows that for native titania layer samples the activity is significantly higher (about 2 orders of magnitude). The existence of an area pathway on  $YSZ/TiO_2/Ni$  samples is not confirmed ( $p = 0.09$  for  $k = 0$ ) Etched samples are only slightly more active than the  $YSZ/Ni$  electrodes. For the etched samples an area pathway could also not be confirmed ( $p = 0.31$  for  $k = 0$ ). Hence ‘TPB’ conductances were calculated by averaging conductances of electrodes and normalizing to  $l_{TPB}$ .

### 3.3.3.3 Activation energy

Since the existence of an area pathway is not certain in both native and etched titania layer samples, only the activation energy of individual electrodes can be evaluated. Figure 3.32 shows the Arrhenius diagram for the measured electrodes for both native and etched titania layer samples with the average fitted activation energy being shown in table 3.2. The figure shows that there

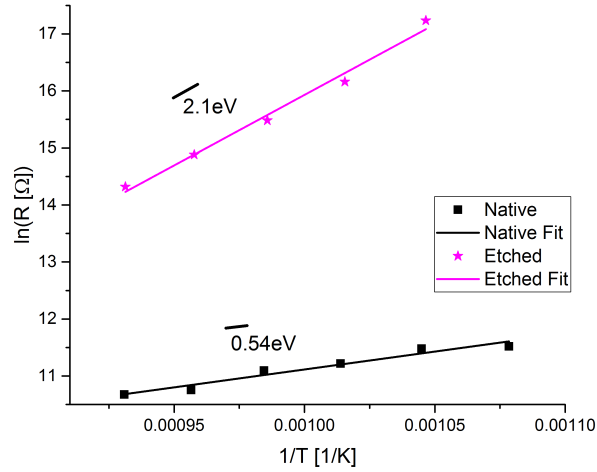


Figure 3.32: Arrhenius diagrams for individual electrodes of native layered and ion etched YSZ/TiO<sub>2</sub>/Ni samples. Atmosphere: 2.5 kPa H<sub>2</sub>/0.15 kPa H<sub>2</sub>O/balance Ar.

is a significant difference between the activation energies of native (0.49 eV) and etched (2.10 eV) titania layer samples.

### 3.3.3.4 Influence of H<sub>2</sub> and H<sub>2</sub>O partial pressures

Similarly to section 3.2.3.4 reaction orders for hydrogen and water were determined for both native and etched titania layer samples. Since an area pathway could not be proven, single electrode data were used instead of separated area/TPB data; the resulting reaction order diagrams are shown in figure 3.33. The figure shows that between the native and etched layer sample a small difference in hydrogen reaction order and a significant difference in water reaction order with a flip of algebraic sign can be found. The existence of an oxygen reaction order is not clear in case of the native layer, while definitely not existing in the etched layer sample.

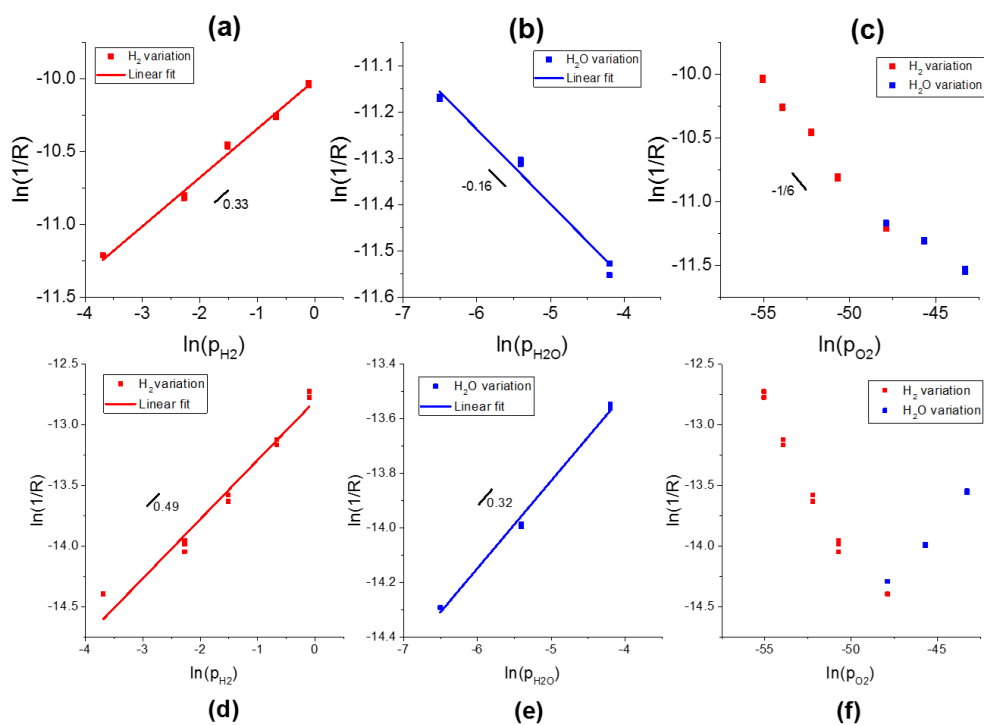


Figure 3.33: Reaction order determination for hydrogen, water, and oxygen on Ni/TiO<sub>2</sub>/YSZ electrodes similar to section 3.2.3.4. a-c Single electrode data for a continuous titania layer sample. d-f Single electrode data for an ion etched sample. Temperature: 800 °C.

### 3.3.3.5 Porous samples

Owing to the very promising results on model-type anodes a simple sol-gel approach was tested with the aim of transferring the improvement effect on the polarization resistance also to porous YSZ/Ni electrodes. For this means, a titania-coating sol was prepared according to Ref. [84]<sup>3</sup>. Porous symmetrical cells (YSZ sheet with symmetrically screen printed YSZ/Ni electrodes, prepared by Plansee SE) were dipped in the sol, dried, and washed with ethanol. Impedance measurements were conducted at standard conditions before and after infiltrating with the titania sol. The resulting impedance spectra are shown in figure 3.34. From the spectra it is evident that infiltration, in contrast to model electrode experiments, did not improve the electrochemical performance.

### 3.3.3.6 Discussion

The comparison of impedance spectra in figure 3.30 shows that extending the titania layer beyond the Ni electrode has a significant effect on the reaction mechanism. This difference is even more impressively shown in figure 3.31 where activities of etched and native titania thin film samples are shown. It can therefore be concluded that a process (e.g. electron, hole, or proton diffusion) extends the reaction zone and thereby increases the activity of the electrode. Since the difference in activity is so pronounced it can rather safely be assumed that any kind of transport co-limitation is not the rate limiting step in etched samples and pure TPB activity of either Ni/ $TiO_2$  or  $TiO_2$ /YSZ can be probed this way.<sup>4</sup> According to this interpretation it can

---

<sup>3</sup>The sol was stirred for only for 4 h here.

<sup>4</sup>Due to the high wetting angle of Ni with ceramics (see YSZ/Ni in figure 3.5) some free titania surface is present, so a contribution of titania surface incorporation cannot completely be excluded.



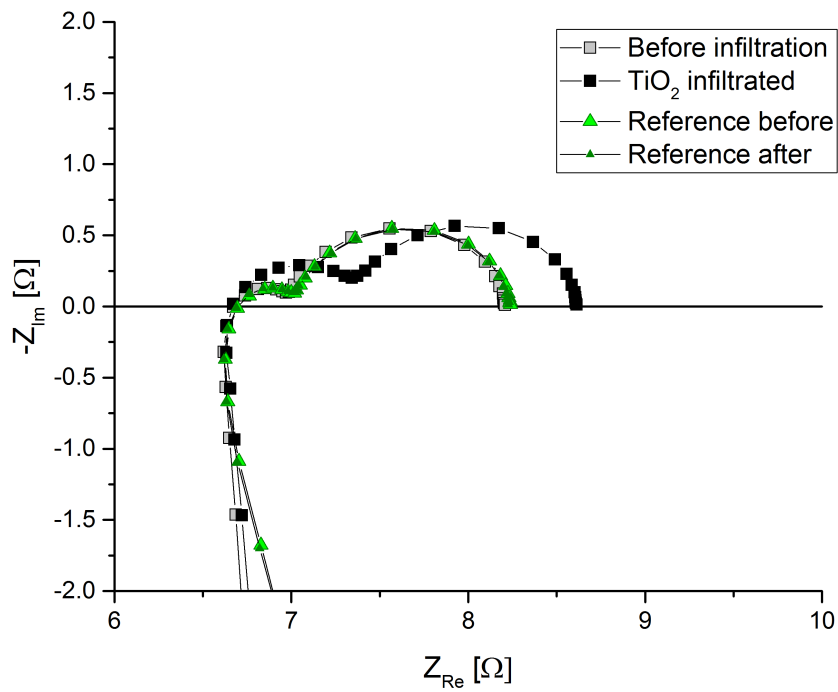


Figure 3.34: Titania infiltration experiment in porous YSZ/Ni cermet electrodes. Additionally to the infiltrated sample a reference sample, which was treated the same except for not being infiltrated with titania sol, is shown to exclude other external effects on the performance. Conditions: 800 °C, 2.5 kPa H<sub>2</sub>/1.5 kPa H<sub>2</sub>O/balance Ar.

be concluded that the TPB reaction has an activation energy of 2.10 eV while the transport reaction has an activation energy of about 0.5 eV (co-limitation with surface incorporation).

Another interesting conclusion that can be drawn from comparing native and etched titania layer samples comes from the reaction order determination, see figure 3.33. Since the only difference between the two samples is the additional lateral charge carrier transport and incorporation in native layer samples the difference in reaction orders can only stem from this additional processes. While the difference is not overly pronounced in hydrogen, the water reaction order is in stark difference, even changing the algebraic sign. With this change there is almost a linear dependency in the reaction order diagram for oxygen. The oxygen reaction order - especially the part derived from the  $p_{H_2}$  variation - would be close to  $-1/6$  (see figure 3.33). This value is also found for the electronic conductance dependency in titania under reducing conditions. [85] It can therefore reasonably be concluded that the lateral transport reaction, which extends the reaction zone, is electron diffusion. Additionally, electronic transport means that in the etched system the active TPB may not be the Ni/TiO<sub>2</sub>/gas TPB, but could also be the TiO<sub>2</sub>/YSZ/gas TPB as electrons are supplied to the electrolyte via the titania phase, not directly via the Ni phase. Which of these two TPBs is indeed active cannot be concluded from available data so far, but would be defined by the relation of ionic and electronic conductance in the titania layer. An attempt to quantify electronic conductivity in titania using Van-der-Pauw 4-point measurements of titania layers on isolating 5 mm x 5 mm MgO substrated was unsuccessful due to the poor conductance of the titania layer. It can hence be assumed that the extended reaction zone described

above does not extend far from the electrode, yet still provides significant catalytic activity.

The infiltration experiment in section 3.34 did not improve the activity of a porous YSZ/Ni cermet electrode, as would be suggested by model electrode results. This discrepancy may be explained by the fact that the microstructure of model electrodes - a layered YSZ/TiO<sub>2</sub>/Ni structure - cannot be reproduced by simply infiltrating titania nanoparticles on an already formed cermet scaffold. Instead of a uniform coating at high temperatures titania particle coagulation may occur which, while still somewhat increasing the activity, mostly just blocks gas diffusion in pores. Transferring model electrode results to application-level cermet electrodes therefore requires a more defined treatment at the powder stage, e.g. by coating YSZ powder with a thin titania shell before preparing the cermet paste. Such studies are, however, far beyond the scope of this thesis.

### **3.3.4 Metal-ceramic variation discussion**

The summary of all relevant results for a comparison of metal-ceramic model electrode systems is shown in table 3.2. Looking at the TPB pathway, the activation energies and hydrogen reaction orders show virtually no difference between the materials (except for YSZ/SSZ/Ni) and the absolute activity values are also within an order of magnitude. (Owing to their different reaction mechanism, native titania layer samples have to be considered separately, see section 3.3.3) Solely the water reaction orders seems to vary based on the metal phase and the type of zirconia. Since in all cases the definite electrolyte is zirconia and the activation energy and activity are similar for the tested material combinations (except for YSZ/SSZ/Ni) the rate limiting step seems to be determined either by the electrolyte phase or impurities.

System	TPB pathway			Area pathway		
	Activity $\text{S m}^{-1}$	Ea eV	RO $H_2$ RO $H_2O$ RO $O_2$	Activity $\text{S m}^{-2}$	Ea eV	RO $H_2$ RO $H_2O$ RO $O_2$
YSZNi	$3.2 \times 10^{-5}$	2.0	0.38 0.35 -	0.21	1.0	0.50 0.35 -
YSZPt	$6.5 \times 10^{-5}$	2.2	0.42 -0.28 -0.19	0.25	1.5	0.50 -0.29 -0.22
YSZSSZNi	$3.8 \times 10^{-5}$	1.6	0.38 0.12 -	0.14	1.1	0.57 -0.04 -
YSZTiO <sub>2</sub> Ni ( <i>etched</i> )	$1.3 \times 10^{-4}$	2.1	0.49 0.32 -	-	-	- - -
YSZTiO <sub>2</sub> Ni ( <i>native</i> )	$7.7 \times 10^{-3}$	0.49	0.33 -0.16 -	-	-	- - -

Table 3.2: Summary of properties of different metal/ceramic electrodes. Activity is the conductance at standard conditions (800 °C, 2.5 kPa  $H_2$ /0.15 kPa  $H_2O$ /balance Ar). It should be noted that for titania samples ‘TPB pathway’ is to be understood loosely (see section 3.3.3).

The impurity hypothesis has the advantage of explaining the significant scattering in activities, activation energies, and reaction orders between studies as the exact chemical environment at the TPB (a region which would be attracting impurity segregation) is expected to vary from study to study because not the exact same impurities were present. Previous studies have also shown that metal purity can indeed affect the electrochemical activity of point electrodes. [43]

Counter to the impurity hypothesis is the fact that YSZ/Ni and YSZ/Pt electrodes share very similar activity, activation energy and hydrogen reaction order. Since SIMS measurements showed that the metal phase is the source of most impurities (see section 3.2.1.3) and it can be assumed that the nickel and platinum targets both have a different impurity profile, a difference in activity would be expected but was not found. Additionally, electrodes in this study have activities which lie between ‘pure’ and ‘impure’ point electrodes in Ref. [43] ( $6.3 \times 10^3 \Omega \text{ cm}$  extrapolated from data in this study to conditions in the reference). This similarity in activity paired with the fact that in this study impurities could not conclusively be found in TEM measurements at the TPB, while an impurity ridge at the TPB was visible in SEM in the reference, appears contradictory to the impurity hypothesis.

These contrary arguments for and against the impurity hypothesis may be reconciled by assuming either no significant influence of impurities in pattern electrodes but a different electrolyte surface<sup>5</sup>, which would be corroborated by the deviant behavior of YSZ/SSZ/Ni samples, or impurities in all electrodes but depending on the exact composition either catalyzing or poisoning properties of the impurity phase at the TPB. Regarding the lacking difference in activity, activation energy and hydrogen reaction order for YSZ/Ni

---

<sup>5</sup>Since Y segregation to the zirconia surface has been shown [62] different amounts of such segregation for differently doped and pre-treated zirconia could be possible.

and YSZ/Pt it would have to be assumed that impurities were introduced during processing of the samples.

# Chapter 4

## Conclusion

In this thesis microstructured thin-film metal electrodes were used to investigate the electrochemical properties of metal/ceramic electrodes. Caution was taken to ensure the maintenance of a dense electrode microstructure at measurement conditions and to obtain electrochemically long-term stable electrodes. The electrodes were further characterized by thoroughly evaluating the geometric properties of each individual electrode and by SIMS and TEM characterization of a sample. A significantly larger number of data points than usual in literature was recorded in order to vindicate clear conclusions from scattering electrochemical data. In sum 73 electrodes of 15 different geometries were evaluated to determine electrochemical properties and particularly to analyze the electrochemical pathways in YSZ/Ni electrodes.

Investigations of the capacitive properties of YSZ/Ni electrodes showed that the absolute value of the capacitance cannot solely be explained by electrostatic models such as the Helmholtz double layer or the Stern model. This discrepancy lead to the conclusion that some ‘chemical’ capacitive mechanism has to be present. This notion was also corroborated by the oxygen chemical potential dependency, the temperature dependency, and the effect of sulfur

exposure on the capacitance. Additionally, the source region of the capacitance was found to be the interface between Ni and YSZ since Ni surface modification did not affect the capacitance and no realistic mechanism was found for a Ni-bulk originating capacitance. Based on the results the most likely source are 2 mechanisms, each dominating at different oxygen partial pressures: At low  $p_{O_2}$  non-stoichiometry in the YSZ or proton storage at the interface are responsible for the capacitance, while at higher oxygen partial pressures analogously to YSZ/Pt in air, oxidation of Ni at the interface (or grain boundaries) causes the high capacitance.

Regarding the catalytic properties of YSZ/Ni it was shown that electrodes with varying  $l_{TPB}$  but constant area have a linear dependency between  $l_{TPB}$  and conductance and that the intercept is statistically significantly larger than zero. This deviation from proportionality is consistent with earlier literature data, though much more reliable. In this study the deviation was further investigated by measuring electrodes with constant  $l_{TPB}$  but varying area. These electrodes showed a linear relationship between area and conductance, which is consistent with an additional parallel reaction pathway scaling with the area. It was shown that these two pathways have different properties such as activation energy, sulfur resilience, and hydrogen reaction orders. Also, two possible reaction mechanisms were proposed for this newly discovered reaction pathway: A ‘proton diffusion mechanism’ in which hydrogen diffuses through the Ni bulk to the YSZ/Ni interface, reacts to a proton, which then diffuses along the interface to the TPB, where it reacts off to water. Alternatively, in the ‘oxide diffusion mechanism’ oxide ions from the YSZ may diffuse through the Ni to the surface, where they react to form water. The former mechanism ties into the above mentioned ‘proton storage’



capacitive mechanism, while the latter ties into the Ni suboxide capacitive mechanism.

The comparison of the TPB pathways of YSZ/Ni, YSZ/Pt, YSZ/SSZ/Ni, and YSZ/etched TiO<sub>2</sub>/Ni samples shows that activity, activation energy, and hydrogen reaction order are surprisingly similar. This similarity, combined with the large scattering of values between authors, indicates a determination of these values either by some impurity phase or differences in the electrolyte surface due to different doping level or pre-treatment. In case of impurities determining the above mentioned properties, it is not straightforwardly possible to simply correlate the amount of impurities to the activity.

For the area pathway some differences in activation energy were found with regards to the metal phase, while the type of zirconia does not seem to have much influence on the corresponding properties. The similarity of the area pathway reaction orders and the TPB pathway reaction orders suggests that parts of the reaction chain are shared for both pathways.

In summary, this thesis showed that micro-structured thin-film model electrodes are a powerful tool for basic research questions, since, contrary to porous cermet electrodes, their geometry can be precisely controlled. Owing to the very large data basis obtained on many electrodes, it was possible to discover previously unknown reaction pathways by geometrical variation of electrode shapes and sizes. It was furthermore possible to compare different material combinations without the uncertainty of a different geometry, providing a starting point for an in-depth understanding of metal/ceramic electrodes, which can improve the future design of SOFC anodes.

# Glossary

$1/R_{Pol}$  Inverse polarization resistance, property indicating electrocatalytic activity [ $S$ ].

$R_{Pol}$  Polarization resistance [ $\Omega$ ].

$l_{TPB}$  Triple phase boundary length [ $m$ ].

# Acronyms

ASC	area specific capacitance.
CPE	constant phase element.
GDC	gadolinium doped ceria.
PLD	pulsed laser deposition.
SEM	scanning electron microscopy.
SIMS	secondary ion mass spectrometry.
SOFC	solid oxide fuel cell.
SSZ	scandia stabilized zirconia.
TEM	transmission electron microscopy.
TPB	triple phase boundary.
YSZ	yttria stabilized zirconia.

# List of Figures

1.1	Schematic drawing of a planar metal supported solid oxide fuel cell fueled with methane. . . . .	3
2.1	General sample preparation workflow. . . . .	15
2.2	Sketch of the electrochemical measurement reactor. . . . .	20
3.1	$l_{TPB}$ vs. area plots for different electrode geometries used in this thesis. . . . .	25
3.2	SEM images of YSZ/Ni electrodes. . . . .	26
3.3	STEM-HAADF image of a YSZ/Ni FIB-lamella. . . . .	28
3.4	STEM-HAADF image of the YSZ/Ni interface. . . . .	29
3.5	STEM-HAADF image of the YSZ/Ni interface and TPB region and EDS spectra of the regions. . . . .	30
3.6	High resolution TEM images of the YSZ/Ni interface and TPB region. . . . .	31
3.7	Lateral ToF-SIMS ion profile of a typical YSZ/Ni electrode after measurement. . . . .	32
3.8	Typical Nyquist plot of a YSZ/Ni impedance spectrum with the two types of fits used in this study. . . . .	33
3.9	Ni microelectrode structure after different treatment. . . . .	36

3.10	Temporal evolution of polarization resistances and capacitances during a long measurement run. . . . .	37
3.11	Effect of the geometry on the YSZ/Ni electrode capacitance. . .	39
3.12	Influence of $H_2S$ on the capacitance of YSZ/Ni electrodes. . .	40
3.13	Influence of bias voltage and oxygen partial pressure on the capacitance of YSZ/Ni electrodes. . . . .	43
3.14	Comparison of capacitances of YSZ/Ni electrodes with/without a YSZ8 top layer. . . . .	44
3.15	Temperature dependence of the capacitance of YSZ/Ni electrodes in an Arrhenius plot. . . . .	44
3.16	Polarization resistance dependence of the TPB length dependency using electrodes with constant area in a double-logarithmic plot. . . . .	52
3.17	Geometry dependency of YSZ/Ni conductance/activity. Inserts show the ideal behavior of solely TPB active electrodes. . .	53
3.18	Area dependent effect of 10 ppm $H_2S$ exposure on electrodes of the geometry series 3 (area variation). . . . .	54
3.19	Temperature dependence of $1/R_{Pol}$ of YSZ/Ni electrodes and pathway specific Arrhenius plot. . . . .	54
3.20	$1/R_{Pol}$ vs. area diagrams for YSZ/Ni electrodes in different atmospheres. . . . .	56
3.21	Reaction order determination for hydrogen and water on YSZ/Ni electrodes. . . . .	57
3.22	Possible reaction mechanism for hydrogen oxidation in YSZ/Ni electrodes. . . . .	62

3.23	Conductance as a function of area for Pt/YSZ electrodes of the geometry series 3 (area variation). YSZ/Ni electrodes are shown for comparison. . . . .	68
3.24	Activation energy determination for Pt/YSZ electrodes analogously to section 3.2.3.3. . . . .	68
3.25	Reaction order determination for hydrogen, water, and oxygen on Pt/YSZ electrodes analogously to section 3.2.3.4. . . . .	70
3.26	Conductance as a function of area for Ni/SSZ electrodes of the geometry series 3 (area variation). YSZ/Ni electrodes are shown for comparison. . . . .	72
3.27	Activation energy determination for Ni/SSZ electrodes analogously to section 3.2.3.3. . . . .	72
3.28	Reaction order determination for hydrogen, water, and oxygen on Ni/SSZ electrodes analogously to section 3.2.3.4 . . . . .	73
3.29	Sketch of titania samples used in this thesis. . . . .	74
3.30	Impedance spectra (Nyquist plots) of Ni/ $TiO_2$ /YSZ electrodes (etched and native). . . . .	75
3.31	Conductance as a function of area for $YSZ/TiO_2/Ni$ electrodes of the geometry series 3 (area variation). . . . .	76
3.32	Arrhenius diagrams for individual electrodes of native layered and ion etched $YSZ/TiO_2/Ni$ samples. . . . .	77
3.33	Reaction order determination for hydrogen, water, and oxygen on Ni/ $TiO_2$ /YSZ electrodes similar to section 3.2.3.4. . . . .	78
3.34	Titania infiltration experiment in porous YSZ/Ni cermet electrodes. . . . .	80

# List of Tables

1.1	Summary of literature results for YSZ/Ni model electrodes, including activation energies, hydrogen and water reaction orders, and the $l_{TPB}$ scaling exponent $\alpha$ . . . . .	13
2.1	Material list. . . . .	18
2.2	Equipment list. . . . .	19
3.1	Fitting results of area-capacitance diagrams shown in section 3.2.2. . . . .	39
3.2	Summary of properties of different metal/ceramic electrodes. . . . .	83

# Bibliography

- [1] F. Birol, Key World Energy Statistics, International Energy Agency, Web Page, **2017**.
- [2] S. Chu, A. Majumdar, *Nature* **2012**, *488*, 294–303.
- [3] A. B. Stambouli, E. Traversa, *Renewable and Sustainable Energy Reviews* **2002**, *6*, 433–455.
- [4] S. J. Lee, S. Mukerjee, E. A. Ticianelli, J. McBreen, *Electrochimica Acta* **1999**, *44*, 3283–3293.
- [5] M. C. Tucker, *Journal of Power Sources* **2010**, *195*, 4570–4582.
- [6] N. Q. Minh, *Solid State Ionics* **2004**, *174*, 271–277.
- [7] S. C. Singhal, *Solid State Ionics* **2002**, *152-153*, 405–410.
- [8] P. Bance, N. P. Brandon, B. Girvan, P. Holbeche, S. O’Dea, B. C. H. Steele, *Journal of Power Sources* **2004**, *131*, 86–90.
- [9] D. Roehrens, F. Han, M. Haydn, W. Schafbauer, D. Sebold, N. H. Menzler, H. P. Buchkremer, *International Journal of Hydrogen Energy* **2015**, *40*, 11538–11542.
- [10] P. Kuchonthara, S. Bhattacharya, A. Tsutsumi, *Journal of Power Sources* **2003**, *117*, 7–13.
- [11] A. Choudhury, H. Chandra, A. Arora, *Renewable and Sustainable Energy Reviews* **2013**, *20*, 430–442.
- [12] A. V. Akkaya, B. Sahin, H. Huseyin Erdem, *International Journal of Hydrogen Energy* **2008**, *33*, 2566–2577.
- [13] S. Ma, J. Wang, Z. Yan, Y. Dai, B. Lu, *Journal of Power Sources* **2011**, *196*, 8463–8471.



- [14] L. Blum, L. G. J. de Haart, J. Malzbender, N. H. Menzler, J. Remmel, R. Steinberger-Wilckens, *Journal of Power Sources* **2013**, *241*, 477–485.
- [15] V. A. Rojek-Wöckner, A. K. Opitz, M. Brandner, J. Mathé, M. Bram, *Journal of Power Sources* **2016**, *328*, 65–74.
- [16] B. Shri Prakash, S. Senthil Kumar, S. T. Aruna, *Renewable and Sustainable Energy Reviews* **2014**, *36*, 149–179.
- [17] D. Sarantaridis, A. Atkinson, *Fuel Cells* **2007**, *7*, 246–258.
- [18] K. Kendall, M. Kendall, *High-temperature solid oxide fuel cells for the 21st century: fundamentals, design and applications*, Elsevier, **2015**.
- [19] M. S. Khan, S.-B. Lee, R.-H. Song, J.-W. Lee, T.-H. Lim, S.-J. Park, *Ceramics International* **2016**, *42*, 35–48.
- [20] Y. Lin, Z. Zhan, J. Liu, S. A. Barnett, *Solid State Ionics* **2005**, *176*, 1827–1835.
- [21] N. Mahato, A. Banerjee, A. Gupta, S. Omar, K. Balani, *Progress in Materials Science* **2015**, *72*, 141–337.
- [22] M. Gong, X. Liu, J. Trembly, C. Johnson, *Journal of Power Sources* **2007**, *168*, 289–298.
- [23] E. Brightman, D. G. Ivey, D. J. L. Brett, N. P. Brandon, *Journal of Power Sources* **2011**, *196*, 7182–7187.
- [24] Z. Cheng, M. Liu, *ECS Transactions* **2013**, *58*, 217–229.
- [25] Z. Cheng, S. Zha, M. Liu, *Journal of Power Sources* **2007**, *172*, 688–693.
- [26] L. Deleebeeck, M. Shishkin, P. Addo, S. Paulson, H. Molero, T. Ziegler, V. Birss, *Physical Chemistry Chemical Physics* **2014**, *16*, 9383–9393.
- [27] K. Haga, S. Adachi, Y. Shiratori, K. Itoh, K. Sasaki, *Solid State Ionics* **2008**, *179*, 1427–1431.
- [28] A. Hauch, A. Hagen, J. Hjelm, T. Ramos, *Journal of The Electrochemical Society* **2014**, *161*, F734–F743.
- [29] J. N. Kuhn, N. Lakshminarayanan, U. S. Ozkan, *Journal of Molecular Catalysis A: Chemical* **2008**, *282*, 9–21.
- [30] N. Lakshminarayanan, U. S. Ozkan, *Applied Catalysis A: General* **2011**, *393*, 138–145.

- [31] O. A. Marina, L. R. Pederson, C. A. Coyle, E. C. Thomsen, D. J. Edwards, *Journal of The Electrochemical Society* **2011**, *158*, B36–B43.
- [32] Y. Matsuzaki, I. Yasuda, *Solid State Ionics* **2000**, *132*, 261–269.
- [33] D. K. Niakolas, *Applied Catalysis A: General* **2014**, *486*, 123–142.
- [34] D. Papurello, A. Lanzini, S. Fiorilli, F. Smeacetto, R. Singh, M. Santarelli, *Chemical Engineering Journal* **2016**, *283*, 1224–1233.
- [35] K. Sasaki, K. Susuki, A. Iyoshi, M. Uchimura, N. Imamura, H. Kusaba, Y. Teraoka, H. Fuchino, K. Tsujimoto, Y. Uchida, N. Jingo, *Journal of The Electrochemical Society* **2006**, *153*, A2023–A2029.
- [36] L. Zhang, S. P. Jiang, H. Q. He, X. Chen, J. Ma, X. C. Song, *International Journal of Hydrogen Energy* **2010**, *35*, 12359–12368.
- [37] J. P. Trembly, A. I. Marquez, T. R. Ohrn, D. J. Bayless, *Journal of Power Sources* **2006**, *158*, 263–273.
- [38] J. F. B. Rasmussen, A. Hagen, *Journal of Power Sources* **2009**, *191*, 534–541.
- [39] H. He, R. J. Gorte, J. M. Vohs, *Electrochemical and Solid-State Letters* **2005**, *8*, A279–A280.
- [40] H. Iwai, N. Shikazono, T. Matsui, H. Teshima, M. Kishimoto, R. Kishida, D. Hayashi, K. Matsuzaki, D. Kanno, M. Saito, H. Muroyama, K. Eguchi, N. Kasagi, H. Yoshida, *Journal of Power Sources* **2010**, *195*, 955–961.
- [41] N. Shikazono, D. Kanno, K. Matsuzaki, H. Teshima, S. Sumino, N. Kasagi, *Journal of The Electrochemical Society* **2010**, *157*, B665–B672.
- [42] Y. Guan, W. Li, Y. Gong, G. Liu, X. Zhang, J. Chen, J. Gelb, W. Yun, Y. Xiong, Y. Tian, H. Wang, *Journal of Power Sources* **2011**, *196*, 1915–1919.
- [43] K. V. Hansen, K. Norrman, M. Mogensen, *Journal of The Electrochemical Society* **2004**, *151*, A1436–A1444.
- [44] K. V. Jensen, R. Wallenberg, I. Chorkendorff, M. Mogensen, *Solid State Ionics* **2003**, *160*, 27–37.
- [45] K. Norrman, K. V. Hansen, M. Mogensen, *Journal of the European Ceramic Society* **2006**, *26*, 967–980.

- [46] A. Utz, K. V. Hansen, K. Norrman, E. Ivers-Tiffée, M. Mogensen, *Solid State Ionics* **2011**, *183*, 60–70.
- [47] A. Utz, H. Störmer, A. Leonide, A. Weber, E. Ivers-Tiffée, *Journal of The Electrochemical Society* **2010**, *157*, B920–B930.
- [48] W. Yao, E. Croiset, *The Canadian Journal of Chemical Engineering* **2015**, *93*, 2157–2167.
- [49] A. M. Sukeshini, B. Habibzadeh, B. P. Becker, C. A. Stoltz, B. W. Eichhorn, G. S. Jackson, *Journal of The Electrochemical Society* **2006**, *153*, A705–A715.
- [50] A. Ehn, J. Høgh, M. Graczyk, K. Norrman, L. Montelius, M. Linne, M. Mogensen, *Journal of The Electrochemical Society* **2010**, *157*, B1588–B1596.
- [51] W. Li, Y. Shi, Y. Luo, Y. Wang, N. Cai, *Journal of Power Sources* **2015**, *276*, 26–31.
- [52] S. Primdahl, M. Mogensen, *Journal of The Electrochemical Society* **1997**, *144*, 3409–3419.
- [53] A. Bieberle, L. P. Meier, L. J. Gauckler, *Journal of The Electrochemical Society* **2001**, *148*, A646–A656.
- [54] D. Kek, M. Mogensen, S. Pejovnik, *Journal of The Electrochemical Society* **2001**, *148*, A878–A886.
- [55] M. G. H. M. Hendriks, J. E. ten Elshof, H. J. M. Bouwmeester, H. Verweij, *Solid State Ionics* **2002**, *146*, 211–217.
- [56] J. Mizusaki, H. Tagawa, T. Saito, K. Kamitani, T. Yamamura, K. Hirano, S. Ehara, T. Takagi, T. Hikita, M. Ippommatsu, S. Nakagawa, K. Hashimoto, *Journal of The Electrochemical Society* **1994**, *141*, 2129–2134.
- [57] J. Mizusaki, H. Tagawa, T. Saito, T. Yamamura, K. Kamitani, K. Hirano, S. Ehara, T. Takagi, T. Hikita, M. Ippommatsu, S. Nakagawa, K. Hashimoto, *Solid State Ionics* **1994**, *70–71, Part 1*, 52–58.
- [58] B. de Boer, Dissertation, University of Twente, **1998**.
- [59] A. Bieberle, L. J. Gauckler, *Solid State Ionics* **2000**, *135*, 337–345.
- [60] M. V. Rao, J. Fleig, M. Zinkevich, F. Aldinger, *Solid State Ionics* **2010**, *181*, 1170–1177.

- [61] W. G. Bessler, M. Vogler, H. Stormer, D. Gerthsen, A. Utz, A. Weber, E. Ivers-Tiffée, *Physical Chemistry Chemical Physics* **2010**, *12*, 13888–13903.
- [62] M. de Ridder, R. G. van Welzenis, A. W. D. van der Gon, H. H. Brongersma, S. Wulff, W.-F. Chu, W. Weppner, *Journal of Applied Physics* **2002**, *92*, 3056–3064.
- [63] A. K. Opitz, J. Fleig, *Solid State Ionics* **2010**, *181*, 684–693.
- [64] C. H. Hsu, F. Mansfeld, *Corrosion* **2001**, *57*, 747–748.
- [65] W. Yao, E. Croiset, *Journal of Power Sources* **2013**, *226*, 162–172.
- [66] M. C. Doppler, J. Fleig, M. Bram, A. K. Opitz, *Journal of The Electrochemical Society* **2016**, *163*, H1019–H1025.
- [67] *NIST Chemistry WebBook, NIST Standard Reference Database Number 69*, National Institute of Standards and Technology, **2005**.
- [68] J. O. Bockris, A. K. N. Reddy, M. Gamboa-Aldeco, *Modern Electrochemistry 2A: Fundamentals of Electrode Processes, Vol. 2A*, 2nd, Springer US, **2000**.
- [69] S. Floreen, J. H. Westbrook, *Acta Metallurgica* **1969**, *17*, 1175–1181.
- [70] G. L. Kellogg, *The Journal of Chemical Physics* **1985**, *83*, 852–854.
- [71] J. Jamnik, J. Maier, *Physical Chemistry Chemical Physics* **2001**, *3*, 1668–1678.
- [72] J. Park, R. N. Blumenthal, *Journal of The Electrochemical Society* **1989**, *136*, 2867–2876.
- [73] N. Sakai, K. Yamaji, T. Horita, H. Kishimoto, Y. P. Xiong, H. Yokokawa, *Solid State Ionics* **2004**, *175*, 387–391.
- [74] H. Yokokawa, H. Kishimoto, K. Yamaji, T. Horita, *ECS Transactions* **2009**, *25*, 2131–2140.
- [75] A. Jaccoud, C. Falgairrette, G. Fóti, C. Comninellis, *Electrochimica Acta* **2007**, *52*, 7927–7935.
- [76] G. Fóti, A. Jaccoud, C. Falgairrette, C. Comninellis, *Journal of Electroceramics* **2009**, *23*, 175–179.
- [77] M. C. Doppler, J. Fleig, M. Bram, A. K. Opitz, *Journal of Power Sources* **2018**, *380*, 46–54.

- [78] A. Hamza, R. Madix, *The Journal of Physical Chemistry* **1985**, *89*, 5381–5386.
- [79] S.-M. Lee, J.-Y. Lee, *Metallurgical Transactions A* **1986**, *17*, 181–187.
- [80] J.-W. Park, C. J. Altstetter, *Metallurgical Transactions A* **1987**, *18*, 43–50.
- [81] F. S. Baumann, J. Fleig, H.-U. Habermeier, J. Maier, *Solid State Ionics* **2006**, *177*, 1071–1081.
- [82] J. Newman, *Journal of The Electrochemical Society* **1966**, *113*, 501–502.
- [83] G. Walch, Thesis, TU Wien, **2016**.
- [84] X. Chao-Hua, J. Shun-Tian, C. Hong-Zheng, W. Mang, *Science and Technology of Advanced Materials* **2008**, *9*, 035001.
- [85] J. Nowotny, M. A. Alim, T. Bak, M. A. Idris, M. Ionescu, K. Prince, M. Z. Sahdan, K. Sopian, M. A. M. Teridi, W. Sigmund, *Chemical Society Reviews* **2015**, *44*, 8424–8442.

# Curriculum vitae

## Personal data

Birth	Feb 9th, 1990 in Krems an der Donau
Citizenship	Austria
Address	Brigittaplatz 14, 1200 Wien, Austria

## Publications

Journal paper	Doppler, M. C., et al. “Hydrogen oxidation mechanisms on Ni/yttria stabilized zirconia anodes: Separation of reaction pathways by geometry variation of pattern electrodes.” <i>Journal of Power Sources</i> 380 (2018): 46-54.
Journal paper	Doppler, M. C., et al. “The Capacitance of Nickel Pattern Electrodes on Zirconia Electrolyte.” <i>Journal of The Electrochemical Society</i> 163.10 (2016): H1019-H1025.
Journal paper	Doppler, M. C., et al. “The influence of sulfur poisoning and YSZ substrate orientation on electrochemical properties of nickel pattern anodes.” <i>ECS Transactions</i> 68.1 (2015): 1383-1390.

Journal paper Szabo, P.S., et al. “Solar Wind Sputtering of Wollastonite as a Lunar Analogue Material – Comparisons between Experiments and Simulation” Icarus (submitted)

## **Education**

03/15-07/18 (est) Doctoral studies

10/12-03/15 Master studies in interdisciplinary masters program “Material Science”

03/10-09/12 Bachelor program “Technical Chemistry”

2004-2009 HBLVA Rosensteingasse

## **Work experience**

01/15-07/18(est) Project member (PhD studies, “CD-Labor für Grenzflächen in metallgestützten elektrochemischen Energiewandlern”)

01/14-05/16 Partner in Michael Doppler OG (Association with Bildungsmanagement GmbH)

09/10-06/12 Tutor at Teaching Support Center, TU Wien

## **Skills & miscellaneous**

Languages	German (native tongue), English (fluent), Mandarin Chinese (HSK3 ~ B1)
Awards	Diploma thesis award of the city of Vienna 2015
Talent program	TUtheTOP 2013/14
IT	Microsoft office, basic knowledge in $\text{\LaTeX}$ (the reader may judge), Python and C dialects, Arduino platform
Interests	Electronics, history, Go/weiqi, juggling

May 8, 2018